The Astrophysical Journal, 929:103 (23pp), 2022 April 10 https://doi.org/10.3847/1538-4357/ac5d46

SolO/EUI Observations of Ubiquitous Fine-scale Bright Dots in an Emerging Flux Region: Comparison with a Bifrost MHD Simulation

Sanjiv K. Tiwari[1,2], Viggo H. Hansteen[1,2,3,4], Bart De Pontieu[1,3,4], Navdeep K. Panesar[1,2], and David Berghmans[5]
[1] Lockheed Martin Solar and Astrophysics Laboratory, 3251 Hanover Street, Bldg. 252, Palo Alto, CA 94304, USA
[2] Bay Area Environmental Research Institute, NASA Research Park, Moffett Field, CA 94035, USA
[3] Rosseland Centre for Solar Physics, University of Oslo, P.O. Box 1029 Blindern, NO-0315 Oslo, Norway
[4] Institute of Theoretical Astrophysics, University of Oslo, P.O. Box 1029 Blindern, NO-0315 Oslo, Norway
[5] Solar-Terrestrial Centre of Excellence-SIDC, Royal Observatory of Belgium, Ringlaan -3- Av. Circulaire, B-1180 Brussels, Belgium
Received 2021 December 7; revised 2022 March 3; accepted 2022 March 10; published 2022 April 18

Abstract

We report on the presence of numerous tiny bright dots in and around an emerging flux region (an X-ray/coronal bright point) observed with SolO's EUI/HRI$_{EUV}$ in 174 Å. These dots are roundish and have a diameter of 675 ± 300 km, a lifetime of 50 ± 35 s, and an intensity enhancement of $30\% \pm 10\%$ above their immediate surroundings. About half of the dots remain isolated during their evolution and move randomly and slowly (<10 km s^{-1}). The other half show extensions, appearing as a small loop or surge/jet, with intensity propagations below 30 km s^{-1}. Many of the bigger and brighter HRI$_{EUV}$ dots are discernible in the SDO/AIA 171 Å channel, have significant emissivity in the temperature range of 1–2 MK, and are often located at polarity inversion lines observed in SDO/HMI LOS magnetograms. Although not as pervasive as in observations, a Bifrost MHD simulation of an emerging flux region does show dots in synthetic Fe IX/X images. These dots in the simulation show distinct Doppler signatures—blueshifts and redshifts coexist, or a redshift of the order of 10 km s^{-1} is followed by a blueshift of similar or higher magnitude. The synthetic images of O V/VI and Si IV lines, which represent transition region radiation, also show the dots that are observed in Fe IX/X images, often expanded in size, or extended as a loop, and always with stronger Doppler velocities (up to 100 km s^{-1}) than that in Fe IX/X lines. Our observation and simulation results, together with the field geometry of dots in the simulation, suggest that most dots in emerging flux regions form in the lower solar atmosphere (at ≈ 1 Mm) by magnetic reconnection between emerging and preexisting/emerged magnetic field. Some dots might be manifestations of magnetoacoustic shocks through the line formation region of Fe IX/X emission.

Unified Astronomy Thesaurus concepts: Solar corona (1483); Solar magnetic flux emergence (2000); Solar magnetic reconnection (1504); Solar extreme ultraviolet emission (1493); Solar transition region (1532); Solar coronal transients (312); X-ray bright point (1812)

Supporting material: animations

1. Introduction

The energy and mass loading of the outer solar atmosphere and the evolution of the magnetic field in emerging or ephemeral magnetic flux regions remain a mystery in solar physics. It is thought that much of the dynamics in emerging flux regions is powered by magnetic reconnection (e.g., Cheung & Isobe 2014; van Driel-Gesztelyi & Green 2015; Moore et al. 2022). The observations of the solar X-ray and extreme-ultraviolet (EUV) corona have revealed heating events in the form of solar explosions of varying magnitudes (e.g., Svestka 1976; Hudson 1991; Masuda et al. 1994; Moore et al. 2001; Aschwanden 2002; Fletcher et al. 2011; Benz 2017). Thus, the energy release events occur from large-scale solar X-ray flares to small-scale EUV dot-like brightenings. New data from Extreme Ultraviolet Imager (EUI; Rochus et al. 2020) on board the mission Solar Orbiter (SolO; Müller et al. 2020) show a plethora of small bright dots that may be signatures of a new field expanding into the upper chromosphere/lower corona with resulting magnetic reconnection and heating.

The emerging ephemeral regions appear in the solar corona as an X-ray bright point, also known as a coronal bright point (CBP; Vaiana et al. 1973; Golub et al. 1974, 1977). These are small bipolar regions of $\sim 40''$, live less than 24 hr, and at a given time have an absolute magnetic flux of 10^{20} Mx or less (Harvey & Martin 1973; Hagenaar 2001; Kontogiannis et al. 2020). Some CBPs might form by magnetic flux convergence and cancellation (Priest et al. 1994; Longcope & Kankelborg 1999). The CBPs are well-studied objects—see Madjarska (2019) for a detailed review. With the availability of high spatial and temporal resolution data, here we are able to investigate "dot-like" substructures inside a CBP.

The presence of numerous fine-scale bright dot-like structures, often referred to as bright grains, in the quiet Sun has been reported in the past in chromospheric and transition region (TR) lines (e.g., Martínez-Sykora et al. 2015). Dots are found to be present in network regions, plage areas, and active regions (Martínez-Sykora et al. 2015; Bryans et al. 2016; Skogsrud et al. 2016; De Pontieu et al. 2017). These chromospheric/TR dots, observed by IRIS (De Pontieu et al. 2014), are mostly roundish, live 2–5 minutes, move with a speed of 30 km s^{-1}, and have a size of 400–2100 km (Skogsrud et al. 2016). The majority of bright grains in weak-field areas

such as in the quiet Sun or coronal holes were proposed to be a result of chromospheric shocks impacting the TR (Martínez-Sykora et al. 2015; Skogsrud et al. 2016). These shocks are driven from the photospheric convection and have been shown to be associated with dynamic fibrils (Skogsrud et al. 2016), commonly observed in Hα (De Pontieu et al. 2007).

Bright dots have also been observed in plage and sunspots in coronal, EUV wavelengths (Régnier et al. 2014; Tian et al. 2014b; Alpert et al. 2016; Deng et al. 2016; Samanta et al. 2017). Sunspot penumbral bright dots were proposed to be caused by magnetic reconnection between more inclined and more vertical penumbral fields (Alpert et al. 2016). Some of these could be linked to penumbral jets and/or Ellerman bombs in sunspot penumbra (Tiwari et al. 2016; Rouppe van der Voort et al. 2021). In plage/moss regions EUV dots were proposed to be nanoflare events (Régnier et al. 2014; see also Testa et al. 2013, 2014, 2020; Winebarger et al. 2013; Polito et al. 2018), in which magnetic reconnection in coronal loops (at apex, or near the chromospheric/TR footpoints) can appear as small localized bursts, rapidly converting magnetic energy into thermal energy (Parker 1988; Priest & Forbes 2000; Aschwanden 2004). Some of these could also be a TR density and temperature enhancement due to the impact of strong downflows along the coronal loops rooted therein (Kleint et al. 2014; Tian et al. 2014b).

Some dot-like fine-scale explosive events having a lifetime of $\sim$1 minute, a diameter (FWHM of the intensity profile across dots) of 800 km, and intensity enhancements of $>$100% were recently reported to be present in the core of an active region (Tiwari et al. 2019) observed by Hi-C 2.1 (Rachmeler et al. 2019). Tiwari et al. (2019) found these dots to be located at polarity inversion lines (PILs). Thus, they proposed those dots to be formed by magnetic reconnection accompanied by magnetic flux cancellation and/or emergence. They also noted the presence of dot-like structures at the base of surges/jets and proposed that some dots could be a part of other, extended explosive events such as tiny loops or surges/jets, reported therein.

Here we present fine-scale dot-like transient brightening events at the location of an emerging magnetic flux region observed by the telescope EUV High Resolution Imager, $\mathrm{HRI_{EUV}}$, of EUI on board SolO. Some of these dots could be considered as the smallest EUV brightenings, or "campfires," recently reported by Berghmans et al. (2021) and Panesar et al. (2021), but earlier by, e.g., Falconer et al. (1998) in the quiet solar corona. We use the commissioning phase data for this study and carefully select 170 dots in the emerging flux region and characterize them by estimating their sizes, lifetimes, and intensity enhancements with respect to their immediate surroundings. We find that dots are present everywhere in the field of view (FOV) of EUI's $\mathrm{HRI_{EUV}}$ 174 Å observations, but they are in an appreciably higher density near stronger-field regions, particularly in the emerging flux region that we investigate here. For a better understanding and interpretations of dots we also synthesize and use images in Fe IX/X, O V/VI, and Si IV emissions from a Bifrost magnetohydrodynamic (MHD) simulation.

2. Data, Methods, and Modeling

We analyze data of a small magnetic flux emergence region that was covered in the quiet-Sun coronal observations of $\mathrm{HRI_{EUV}}$ on 2020 May 20 (Figure 1). As evident from the Hinode/X-Ray Telescope (Golub et al. 2007) image in Figure 1(c), the emerging flux region is a classical X-ray/coronal bright point. Line-of-sight (LOS) magnetograms (Figures 1(d)–(f)) and a flux evolution plot (Figure 1(g)) provide further evidence of this region being a CBP with short-closed loops therein. We use calibrated L2 EUI data (Kraaikamp et al. 2020) for our study. The L2 data product is the calibrated data, suitable for scientific analysis. The $\mathrm{HRI_{EUV}}$ wavelength passband ranges from 171 to 178 Å and is centered on 174 Å. Thus, the EUI 174 Å channel detects the characteristic emissions of the Fe IX and Fe X lines from the coronal plasma at about 1 MK. The EUI 174 Å passband also includes O V/VI lines and thus detects some TR emission, presumably—see more discussion on this later. The plate scale of EUI data used in the present analysis is 0.″492. The SolO/EUI was situated at 0.609 au from the Sun on 2020 May 20; thus, 1 $\mathrm{HRI_{EUV}}$ pixel corresponds to about 217 km on the Sun, with a resultant 2-pixel Nyquist spatial resolution of 434 km.

The telescope $\mathrm{HRI_{EUV}}$ obtained 174 Å images between 21:20:12 and 22:17:02 UT, cycling through a 2-minute program. During this period, $\mathrm{HRI_{EUV}}$ took five images at a 10 s cadence plus a sixth image 70 s later. Thus, SolO provided the $\mathrm{HRI_{EUV}}$ images with aforementioned temporal cadence for about 57 minutes. These observations were taken as part of a technical compression test of $\mathrm{HRI_{EUV}}$. Therefore, these images have variable settings. Nonetheless, during the 57-minute observations 60 images were well exposed, unbinned, and compressed at high-quality levels. Our analyzed data frames are from within these 60 high-quality images. We have used a cross-correlation technique to co-align $\mathrm{HRI_{EUV}}$ images with each other. However, because of the variable compression, the co-alignment using the cross-correlation method has not been straightforward, and thus the co-alignment cannot be considered perfect.

Because of the usual enhanced brightness in coronal loops in the emerging flux region, dots mostly appear faint. Therefore, we created unsharp masked images, from $\mathrm{HRI_{EUV}}$ 174 Å images, to enhance the visibility of dots; see e.g., Figure 2. For this purpose we subtracted smoothed frames (by a factor of 5 pixels) from the original data. We have prepared movies of $\mathrm{HRI_{EUV}}$ 174 Å images and unsharp masked images, available as an online animation (Figure 2). In the movie we have kept all image frames available during the 57-minute observations, for reference, and have not removed binned and/or bad frames.

We also use EUV data obtained with Atmospheric Imaging Assembly (AIA; Lemen et al. 2012), on board Solar Dynamics Observatory (SDO; Pesnell et al. 2012), and LOS magnetograms from the Helioseismic and Magnetic Imager (HMI; Scherrer et al. 2012; Schou et al. 2012), also on board SDO. A similar unsharp masking, using 5×5 AIA pixels, is applied to AIA 171 Å images. Note that SolO was at 0.609 au from the Sun on 2020 May 20; therefore, the events would appear 3.22 minutes earlier in SolO/EUI images than in the SDO/AIA images. The angle between SolO and the Sun–Earth line on 2020 May 20 was 16.°4. All our generated maps ($\mathrm{HRI_{EUV}}$, AIA, and HMI) were processed and de-rotated using SolarSoft routines (Freeland & Handy 1998). The reference frame for de-rotation is the central image in our SDO data, i.e., at 2020 May 20 21:44:51 UT. A roll angle correction of 6° is made to match that with SolO/EUI. The solar (X, Y) SDO coordinates at the reference time are as follows: xrange = [300, 365], yrange = [53, 118]. The magnetograms are within 30° from

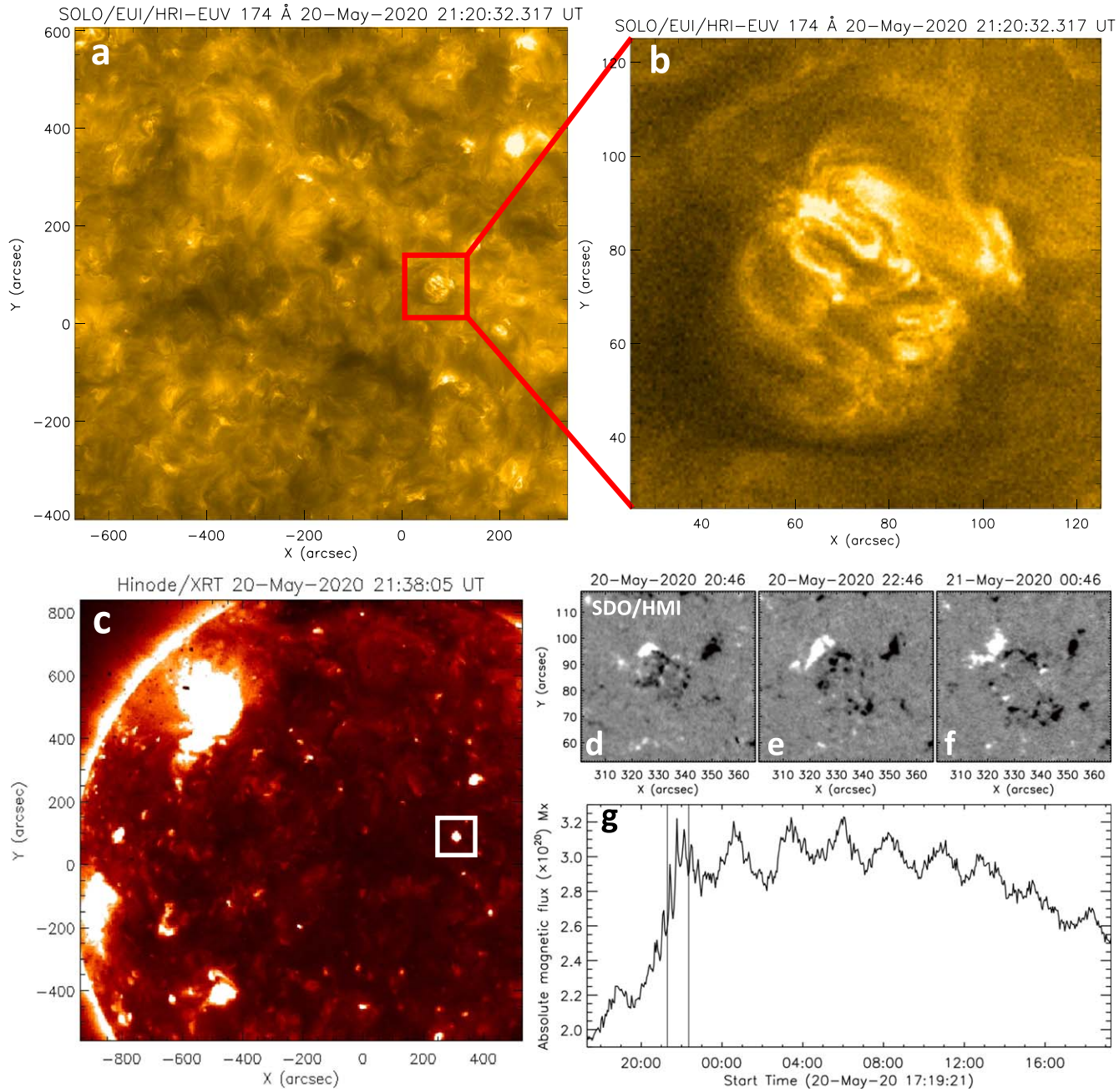

Figure 1. A context image (panel (a)) of the full FOV observed by HRI_{EUV} on 2020 May 20 at 21:20:32 UT. An emerging flux region is outlined by a red box, an enlarged version of which is displayed in panel (b) and used for analyzing fine-scale dots. One arcsecond of the HRI_{EUV} data on 2020 May 20 covers 442 km on the Sun. Panel (c) shows an Hinode/XRT image in which the emerging region, outlined by a white box, appears as an X-ray/coronal bright point. Panels (d)–(f) display three maps of SDO/HMI LOS magnetic field of the emerging flux region, the magnetic flux of which over 24 hr is plotted in panel (g). The two vertical lines in panel (g) outline the duration of HRI_{EUV} observations. In all panels in this figure, as well in all other images in the paper, solar north is up, and solar west is to the right.

the disk center, and therefore a projection effect correction is not essential (see, e.g., Falconer et al. 2016). A movie containing AIA 171 Å images and its unsharp masked images, together with HMI LOS magnetograms, corresponding to Figure 4, is available online.

2.1. Selection Criterion of Dots

We employ two criteria for selecting dots: (i) We select a quieter region in the surroundings of the emerging region (e.g., outlined by a dashed white box in Figure 2) and estimate the mean value of the intensity and its standard deviation inside the box, which is considered the 1σ noise level. We select dots that have an intensity enhancement above the 2σ level from their surroundings. For example, if 1σ of the quiet region is 8% of the mean for an image frame, all selected dots in that image frame should have intensity enhancements above 16% of their immediate surroundings. (ii) The dot should be visible in at least two consecutive image frames. Thus, if a dot is at or above 2σ level intensity from their immediate surroundings and is visible in two or more consecutive image frames, the dot has been considered for analysis. This ensures that the selected dots are not noise.

However, we have considered a few exceptions. We found a few striking dots to be above the 3σ intensity level of their

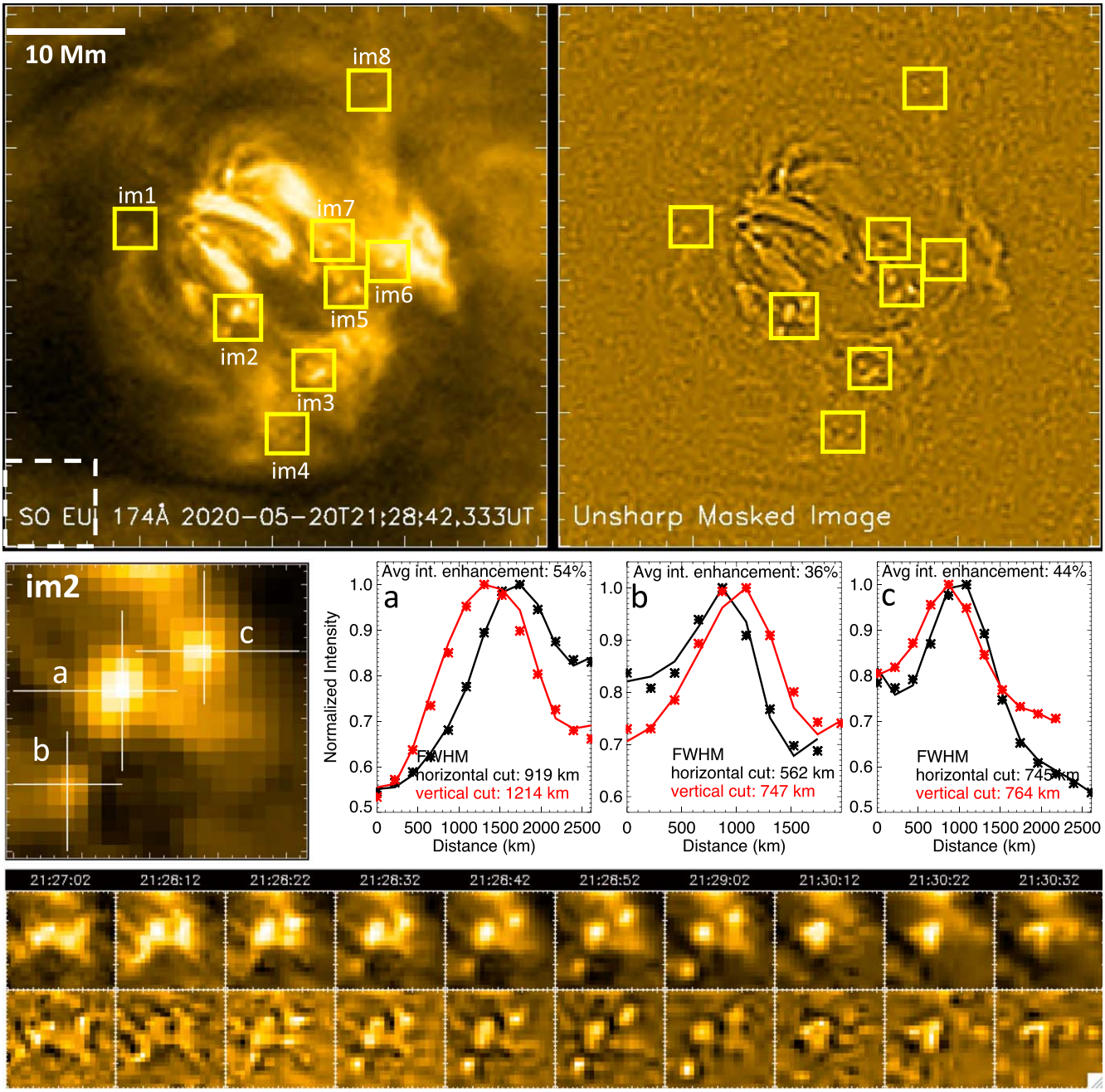

Figure 2. Examples of fine-scale dots in EUI/HRI_{EUV} observations. Top row: the left panel is an HRI_{EUV} 174 Å image of the same FOV as in Figure 1(b), and the right panel is an unsharp masked image of it. Different boxes outline the regions of selected dots in this image frame. A white dashed box in the lower left corner outlines the region that is used for noise estimation. A white horizontal bar in the top left corner scales 10 Mm distance, for reference. Middle row: on the left is a zoomed-in view of one of the boxed regions, named "im2," of the same time as that in the top row. This region has three dots, named a, b, and c. The sizes along the horizontal (in black) and vertical cuts (in red) of these dots, together with their Gaussian fits (asterisks), are shown in the right three panels. The profile plots are on the original HRI_{EUV} images. The brightness enhancement of each dot with respect to their immediate surroundings is also printed. Bottom row: time series images, together with the corresponding unsharp masked images, of the region outlined by box "im2" are shown to follow the evolutions and lifetimes of the three dots a, b, and c. Note that the images are not isochronal. This is because this HRI_{EUV} data set was taken as part of a compression test, as described in Section 2. An animation of the uppermost row is available online. The movie has the same FOV but no annotations, and it runs (in SolO time) from 21:20 to 22:17 UT.

(An animation of this figure is available.)

surroundings but visible in only one image frame, thus having a lifetime of less than 10 s. We have included those.[6]

Similarly, a few dots whose intensity enhancement is slightly below or close to the threshold 2σ value but that are visible in two or more consecutive image frames are also included. Together, these dots represent less than 10% of our sample. The reason for including these is that these dots are most likely real, but they do not satisfy the criterion, either because of a lower cadence of the data than their lifetimes, or due to them not being strikingly bright with respect to their surroundings, which are also bright. Another factor that we considered for keeping these dots in our sample is that, as mentioned above, there is a 70 s gap after five consecutive

[6] There is no way to rule out the possibility of these dots being the effect of cosmic rays. Nonetheless, these dots present less than 5% of our sample and do not affect the main results.

image frames, which complicates finding the true lifetimes of dots.

The selected dots are isolated enough from other dots and bright structures in their surroundings to characterize them more accurately. Dots are mostly roundish (unlike penumbral dots (see, e.g., Tian et al. 2014b; Alpert et al. 2016), which are often extended along sunspot penumbral filaments; Tiwari et al. 2013). Thus, we take horizontal and vertical cuts for measurement of the size of dots. Even when dots are extended in a direction, there is no preferred direction. On the one hand, this suggests that the dots in the emerging flux region might be different from the "elongated" dots in the sunspot penumbra. On the other hand, this also implies that any dot extensions would not be caused by camera artifacts. We therefore keep it simple by measuring distances along two cuts (in horizontal and vertical directions) and then averaging them to extract the diameter of each dot. We selected and characterized each of the dots in HRI_{EUV} manually because the dots are usually dim with respect to their surroundings, and the HRI_{EUV} pointing is not always stable during this commissioning phase, so that automatic selection of these fine-scale dots would fail and/or give erroneous results.

2.2. Bifrost MHD Model

We use a Bifrost MHD simulation of an emerging flux region. This is a new simulation in that we have modeled the quiet-Sun network/an emerging magnetic flux region by injecting a horizontal flux sheet of time-varying strength at the bottom boundary of a model that spans a domain of $72 \times 72 \times 61$ Mm^3 on a grid of [720, 720, 1115] grid points using the Bifrost code (Gudiksen et al. 2011). The model reaches from 8.5 Mm below the photosphere and extends into the corona, up to 52.5 Mm above the photosphere. The Bifrost model includes optically thick radiative transfer, including scattering in the chromosphere (see, e.g., Skartlien 2000; Hayek et al. 2010), and optically or effectively thin radiative transfer in the middle chromosphere to corona following the recipes of Carlsson & Leenaarts (2012). The equation of state, including partial ionization of the atmospheric plasma, is treated in local thermodynamic equilibrium (LTE) through a look-up table constructed using solar abundances. Furthermore, thermal conduction along the magnetic field, especially relevant for the corona, is included in the energy equation.

The model is initialized with a horizontal field of 100 G up to the photosphere, with a nearly 0 G field in the corona. This is evolved with an initial field injection of $B_y = 200$ G at the bottom boundary for 95 minutes. Convective dynamics lead to a tangled field and a hot corona >1 MK after an hour of solar time. At 95 minutes the field strength of the flux sheet entering the bottom boundary was increased to $B_y = 1000$ G for 70 minutes, followed by another increase to 2000 G for the next 150 minutes. After this strong field injection is completed, the field strength injected was reduced to $B_y = 300$ G, at which point it remains constant. After the first hour or so, most coronal transients have dissipated and the photospheric field closely resembles the measured photospheric field in observations (V. H. Hansteen et al. 2022, in preparation). The first signs of flux emergence occur at (roughly) 3 hr, but this may be convectively processed ambient field breaking through the photosphere. Field stored just below or rising to the photosphere will break through the surface and enter the upper atmosphere once the gradient of the subphotospheric field strength becomes sufficiently large (Archontis et al. 2004). Stronger flux emergence occurs at later stages in the simulation —this phase of the simulation is featured in this paper, which is suitable for comparison with the emerging flux region of HRI_{EUV} observations used in this study.

For line synthesis, we calculate their emission by integrating the contribution function $\phi(u, T)n_e n_H G(T, n_e)$ along the LOS, where ϕ is the emission profile, n_e and n_H are the electron and hydrogen number densities, respectively, and $G(T, n_e)$ is a function describing the ionization and excitation state of the emitting ion taken from CHIANTI (Dere et al. 1997). The latter assumes the ionization and excitation equilibrium. This integration is performed using CUDA, i.e., a parallel computing platform developed by NVIDIA for computing on graphical processing units (GPU), which accelerates the integrations drastically. Since the wavelengths of the iron lines are short, there is the possibility of absorption from neutral gas. We include this effect in our calculation by multiplying the contribution function along the LOS with $\exp(-\tau)$, where τ is the combined opacity of hydrogen and helium, as well as from singly ionized helium (see De Pontieu et al. 2009, for details).

3. Results

3.1. Dots in EUI Observations

In Figure 2 we display an example HRI_{EUV} image frame and its unsharp masked image. Many of the fine-scale dots are discernible. Some of the outstanding dots are outlined by yellow boxes. The dots are particularly clearly visible in the unsharp masked image. Many more fine-scale dots are outlined in Appendix A in two additional image frames from the HRI_{EUV} movie of the emerging flux region (Figure 2). We manually selected 170 dots from different image frames of the animated Figure 2 and characterized them by calculating their sizes, lifetimes, and intensity enhancements with respect to their immediate surroundings. Most of the fine-scale dots are roundish in the image frame when they are selected for analysis. While half of the dots remain roundish during their lifetimes, the other half of dots extend, sometimes explosively, to become a loop or a jet/surge-like event (see examples in Figure 2). Sometimes a dot splits into two or more dots, and occasionally two or more dots merge to become a single dot or a slightly extended structure.

The estimation of intensity enhancements of dots with respect to their background is done by averaging the minimum intensity values at each end of the two intensity profiles, separately, that are used for assessing the horizontal and vertical sizes of dots. Then, we evaluate what percentage of this averaged value, for each profile, is the peak intensity value. An average of these two percentage numbers (from the two intensity profiles) is the percentage brightness enhancement of a dot with respect to its immediate surroundings. The following general caveat should be kept in mind when interpreting and/or comparing the percentage intensity enhancement of different dots from their immediate surroundings (as measured here, and generally done in the studies cited in this paper): the percentage intensity increase depends on the background, which can be different from instrument to instrument (affected by, e.g., stray light, the telescope's point-spread function (PSF)), from wavelength to wavelength, and from environment (active region, ephemeral region, quiet Sun) to environment.

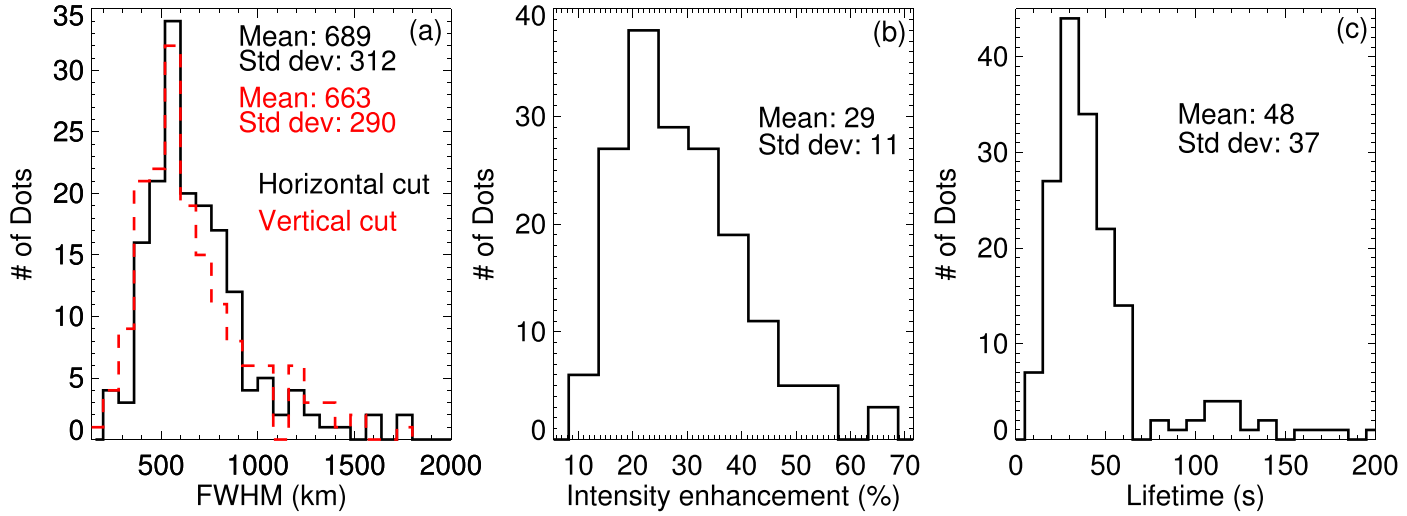

Figure 3. Histograms of the sizes, intensity enhancements, and lifetimes of 170 dots observed with HRI_{EUV}. Panel (a) shows histograms of the horizontal and vertical sizes of dots. Panel (b) shows the histogram of intensity enhancements with respect to the immediate surroundings of dots. Panel (c) displays the histogram of lifetimes of dots.

In Figure 2, we also display three dots "a," "b," and "c" from inside the box "im2" more closely. Dot "a" is the biggest (diameter ∼1000 km) and brightest (54% brighter than its immediate surroundings) of the three and extends toward the south, becoming a jet-like activity. Dot "b" is the smallest (diameter ∼650 km) and dimmest (36% brighter than its immediate surroundings) of the three and remains mostly isolated until its disappearance. Dot "c" appears to originate from a longer bright loop-like structure in its south (see the image at 21:28:12 UT).

Intensity enhancements might be considered underestimated to some extent owing to the fact that we have taken averages of the intensities of four locations/pixels at minimum intensities for the two cuts (horizontal and vertical) and have not taken averages of many more pixels in the surroundings that could have lower values than the four points along the two cuts, particularly because most of the emerging region is bright, in general.

For the lifetime of each dot we follow the dot manually in a zoomed-in region and visually find out the time between when the dot looked like a dot and when it disappears, or becomes another feature such as a loop or a jet/surge. Examples of the estimation of the lifetimes of three dots are described in the last row of Figure 2.

3.1.1. Statistical Properties of HRI_{EUV} Dots

We performed a statistical quantitative analysis of the physical properties of dots observed by HRI_{EUV} and created their histograms. The histograms of the sizes, lifetimes, and intensity enhancements of 170 dots are displayed in Figure 3. Most dots have a diameter of about 800 km or less. Thus, most dots are fairly small in size. But some dots can have a diameter of as large as 2000 km, or more. The averages of horizontal and vertical sizes of the 170 dots come out to be 689 ± 312 km and 663 ± 290 km, respectively. Although some dots appear extended in one direction (during their measurements—when they are most circular), evidently the dot's horizontal and vertical sizes are not significantly different. Thus, the average diameter of the dots in our sample is 676 ± 301 km.

Most dots have an intensity enhancement of 20%–40% to their immediate surroundings, with an average of $29\% \pm 11\%$. Because our dots are dim, many of these dots are not so clearly visible in direct HRI_{EUV} 174 Å images and become clearer in the unsharp masked images. The intensity enhancement of dots is rather low as compared to the previously reported numbers of brightness enhancements for EUV dots in the literature. For example, these numbers are fairly low as compared to that of the dots reported in the core of an active region using Hi-C 2.1 data, which have intensity enhancements of $\geqslant 100\%$.[7] But again, remember the caveat mentioned in Section 3.1 on how the estimation of percentage intensity enhancement can be affected by different magnetic backgrounds, wavelengths, and instruments.

The dots are fairly short-lived. The lifetime of most dots is below a minute, but some can be longer-lived, up to 3 minutes or more. Most dots in the previous literature have longer lifetimes, on average, than the dots reported here. The average lifetime of our HRI_{EUV} dots is 48 ± 37 s, which can be considered as the upper limit for average duration of dots. This is because, as described in Section 2, the HRI_{EUV} images are not isochronal, so that if a dot's lifetime is longer than 70 s we cannot be sure whether it is the same event or there are two subsequent events.

We also measured the plane-of-sky speeds of a few dots that show considerable proper motions. We also calculated the speeds of brightness propagation along a dot's extension by creating time–distance maps in the way described later in Section 3.3.2; see Figure 11. Most dots show random and slow proper motions of about 2–10 km s^{-1}. The brightness propagation along a dot's extension can have a speed of up to 30 km s^{-1}. Because most dots show a little proper motion, and there are some image alignment issues in the commissioning phase data, it is often difficult to track and quantify the speeds of fine-scale structures such as dots. Note that a proper motion of 2 km s^{-1} is comparable to the displacements caused by uncertainty in the image alignment.

[7] Please note that the brightness enhancements for Dot 1 and Dot 2 in Figure 3 of Tiwari et al. (2019) (and any corresponding text) should read as 120% and 435%, respectively, which were inadvertently given as of 60% and 80%.

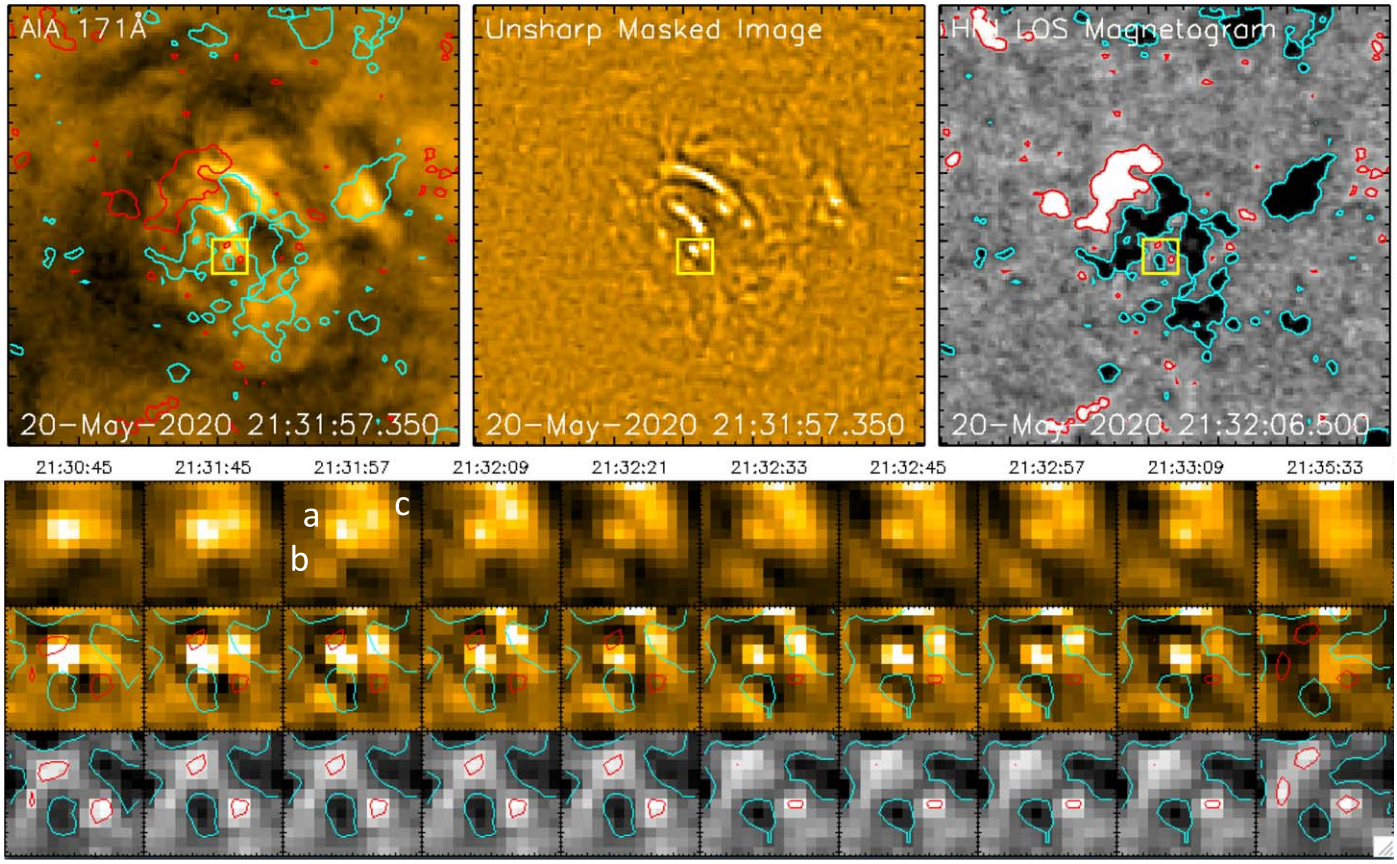

Figure 4. SDO observations of the same emerging flux region for the corresponding time of the HRI_{EUV} image displayed in Figure 2. The top panel shows, from left to right, the AIA 171 Å image, its unsharp masked image, and the HMI LOS magnetogram, respectively. The (*X*, *Y*) coordinates are the same as in Figures 1(d)–(f). A yellow box outlines the same region as im2 in Figure 2. The AIA 171 Å image and LOS magnetogram have HMI LOS magnetic field contours (of the same time) of level ±20 G overlaid—red is for positive magnetic polarity, and cyan is for negative magnetic polarity. The LOS magnetogram is saturated at ±40 G. The bottom panel shows the evolution of the same three dots a, b, and c, as in Figure 2, but here as seen from SDO/AIA. The last row of the bottom panel contains corresponding LOS magnetic field evolution together with its contours from SDO/HMI. An animation is available online. Its annotations and FOV are the same as in the top panel of the figure, and it runs from 21:20 to 22:20 UT at a 12 s cadence.

(An animation of this figure is available.)

3.2. Dots in SDO Observations

We manually co-aligned SDO (AIA and HMI) data with EUI HRI_{EUV} data to allow tracking of fine-scale EUI dots in AIA 171 Å images. We found that many of the HRI_{EUV} dots are discernible in SDO/AIA 171 Å images. Because the angle between LOS directions of SolO and SDO during our observations was only 16°.4, there was no foreshortening correction made. These dots obviously exceed 1 AIA pixel, similar to campfires (e.g., Rutten 2020; Berghmans et al. 2021; Panesar et al. 2021).

We followed the evolution of magnetic flux, underlying the dots, in HMI LOS magnetograms. Figure 4 shows an AIA 171 Å image and its unsharp masked image, nearly at the same time as the HRI_{EUV} image in Figure 2. The difference in the noted times in the two images (EUI image is 195 s earlier than AIA) is due to the difference in the distance of the two spacecraft from the Sun. The HMI LOS magnetogram of the nearest time to the AIA 171 Å image is also shown, with magnetic contours overplotted on it. The contours are also overplotted on the AIA 171 Å image to allow easy tracking of magnetic polarity distribution underlying the dots. Because these dots are often dim in AIA 171 Å and are not as outstanding as they are in HRI_{EUV} 174 Å images, these were not reported and particularly explored in emerging flux regions in the past in AIA observations.

The three dots ("a," "b," and "c") in the AIA 171 Å image, outlined by a yellow box in Figure 4, are the same as those shown inside box "im2" in Figure 2 observed with HRI_{EUV}. Although the dots are not so obvious in AIA 171 Å images, these and many of the other bigger and brighter HRI_{EUV} dots become discernible in the unsharp masked images of the SDO/AIA 171 Å channel. In Figure 15, we display images of the same FOV as in Figure 4, in several AIA channels. We find faint signatures of dots "a," "b," and "c" in AIA 304, 193, and 131 Å images, similar to that seen in the AIA 171 Å image. A distinct signature of these dots cannot be seen in AIA 1600 and 1700 Å images. These together further suggest that many, if not all, dots are TR feet of coronal loops.

The bottom row of Figure 4 shows that mixed-polarity magnetic flux is present near the dots "a" and "c"—emerging minority-polarity (positive) magnetic flux eventually cancels with preexisting majority-polarity (negative) magnetic flux. The movie in Figure 4 with AIA and HMI data shows that the biggest dots, such as dot "a" in Figure 4, are often seated at or near sharp neutral lines, and apparent emergence and cancellation of minority-polarity magnetic flux are seen. This behavior of magnetic field distribution is similar to that seen for Hi-C 2.1

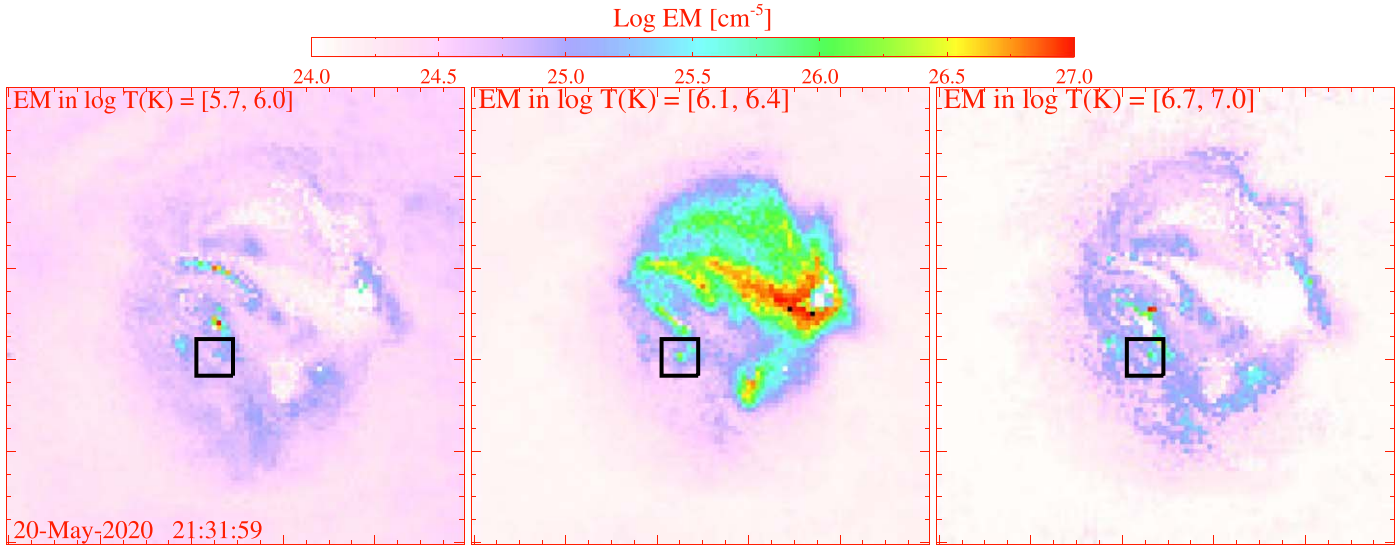

Figure 5. The EM maps, of the same FOV as the AIA 171 Å image in the top panel of Figure 4, in three log temperature ($\log_{10}T$) bins. The black box outlines the same region as im2 in Figure 2, and also outlined by a yellow box in SDO images in Figure 4, covering dots "a," "b," and "c". Two ("a" and "c") of the three dots apparently have significant EM in the temperature range of 1–2.5 MK. The third one (dot "b") does not have significant emission in any of the temperature ranges shown.

dots in the arch filament system in the core of an active region by Tiwari et al. (2019), who also found flux cancellation rates of the order of 10^{16}–10^{17} Mx s^{-1} for some of their fine-scale explosive events. Note that there is no signature of mixed-polarity magnetic flux near dot "b." This could be due to the opposite-polarity flux elements being beyond the detection limit of HMI. Alternatively, dot "b" might not form the same way as dots "a" and "c."

Similar to that what is seen in the $\mathrm{HRI_{EUV}}$ images during the evolution of dots, we also note that the dots in AIA images show extensions as a loop, or a jet, mostly during their later phase, but occasionally dots also form at the end of an explosion (from a more extended, jet-like or loop-like structure).

3.2.1. Differential Emission Measure

To determine the emission of dots in different temperature bins, we performed differential emission measure (DEM) analysis by using six AIA channels (171, 211, 335, 193, 94, and 131 Å) following the method described in Cheung et al. (2015). In Figure 5, emissivities for three temperature bins are displayed at approximately the same time as for the images in Figures 2 and 4. Two ("a" and "c") out of the three dots outlined by the box in Figure 4 (which are the same ones from $\mathrm{HRI_{EUV}}$ inside box "im2") show emissivity in the temperature bin of $\log_{10}T = [6.1, 6.4]$. The third, the smallest dot in the south (named "b"), does not show any emission in any of the T bins. Thus, this dot could be at a cooler chromospheric/TR temperature. However, the two larger dots are evidently heated to a coronal temperature of 1 MK or more.

We performed this analysis on several AIA image frames corresponding to $\mathrm{HRI_{EUV}}$ observations and found similar results. The biggest and brightest dots show up in the temperature range of 1–3 MK, or sometimes even at higher temperatures. However, the dimmer and cooler ones are not visible in the 1 MK or higher temperature bins. A caveat is that because of the limited temperature sensitivity of the low/TR temperatures in the AIA channels, the TR contributions to the AIA passbands are relatively poorly constrained. Further, dots are so short-lived that a statistical equilibrium assumed in the DEM analysis might not be valid.

3.3. Dots in Bifrost MHD Simulation—Synthesized Fe IX/X Emissions

We use synthesized Fe IX and Fe X emissions from the Bifrost simulation, described in Section 2.2, and calculated the line intensities, Doppler speeds v_{Dopp}, and vertical component of the magnetic field Bz. We mainly chose Fe IX and Fe X lines because these are the pivotal lines in the $\mathrm{HRI_{EUV}}$ 174 Å passband. The Fe IX 171 Å and Fe X 174 Å are optically thin lines. To keep the similarity with the EUI observations, we averaged synthetic Fe IX and Fe X emissions to make a single Fe IX/X map that is then used for the analysis. We also averaged Dopplergrams of the two lines for consistency. We used the simulation frames from 420 (∼5.8 hr after the start) to 567 (∼7.8 hr after the start) at a 50 s cadence. We use these frames because these appear to match best with the magnetic field evolution in the early phase of the flux emergence that is captured by the $\mathrm{HRI_{EUV}}$ observations used here. The pixel size of the simulation is 100 km.

In Figure 6, an example frame of the simulation containing an Fe IX/X emission image, its unsharp masked image, Bz, and v_{Dopp} map are shown, all in top-down vertical simulation viewing. Several of the outstanding dots are outlined by yellow (black in Dopplergrams) boxes. Details of Bifrost dot Dopplergrams can be found in Section 3.3.3. We investigated 30 dots in detail and find that, similar to those in the observations, half of the dots in the simulation show extension during their evolution, to become a loop- or jet-like activity. We estimated the sizes, lifetimes, and intensity enhancements of dots from their immediate background in the same way as done for the dots in $\mathrm{HRI_{EUV}}$ observations, and we plotted their histograms in Figure 7. For a reasonable comparison, we have estimated lifetimes, sizes, and brightness levels on the synthetic Fe IX/X data after smearing them to the EUI resolution. Nonetheless, as we did not use the telescope's PSF to smear the synthetic images, the comparison is still not completely fair.

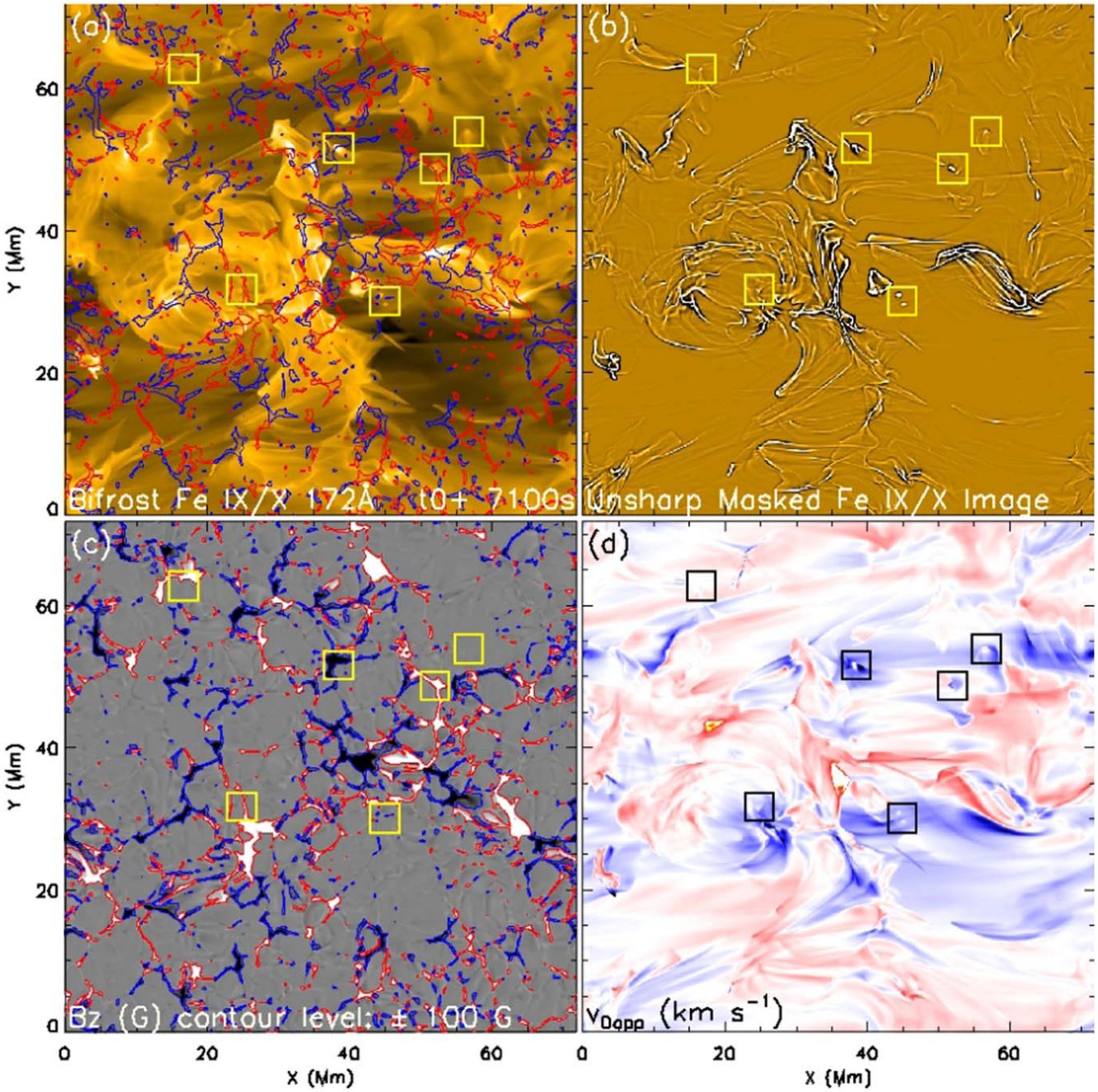

Figure 6. Images of three physical parameters from the Bifrost MHD simulation of an emerging bipolar region: (a) synthesized Fe IX/X emission; (b) unsharp masked image of panel (a); (c) surface Bz map, saturated at ±500 G; and (d) Fe IX/X Doppler shift, v_{Dopp} (representing the observable), with the upper and lower values saturated at ±50 km s^{-1}. The contours (of ± 100 G) of the magnetogram are overplotted in panels (a) and (c). A few dots are outlined by yellow boxes (black in Dopplergrams), for examples.

We find the sizes of dots in the simulation (487 km, on the average) to be about 28% smaller, on the whole, than that found for dots in HRI_{EUV} observations (see Figures 3(a) and 7(a)). Partly this could be due to not using the telescope's PSF to smear the synthetic images to HRI_{EUV} spatial resolution. The lifetimes of dots in the simulation are on the higher end from the observations —most dots in the simulation live 50–100 s. Some appear only in a frame and have a lifetime of less than 50 s. Please note that the lower limit of the lifetime of dots is the cadence of our simulation, i.e., 50 s. The intensity enhancements of the dots from their surroundings vary significantly. For most dots the brightness level is several hundred percent from their immediate surroundings, with an overall average of 500%. This is much higher than the intensity enhancements of the dots in the emerging flux region of HRI_{EUV}, but it is of the order of the brightest Hi-C 2.1 dots (found in the core of an active region; Tiwari et al. 2019). In Figures 8 and 9 we show the evolution of different physical parameters of five example dots. Dot 1 is an isolated dot that remains roundish throughout. Dot 2 is also an isolated dot but extends briefly to become a loop-like (or jet-like when seen in O V/VI and Si IV lines) structure. This dot presents the most obvious mixed-polarity magnetic flux at its base. Dot 3 is mostly isolated and splits into two before disappearing. Dot 4 is initially a loop- or surge-like brightening, extended in the south, that contracts to become a dot. Dot 5 explodes to become a surge/jet-like activity.

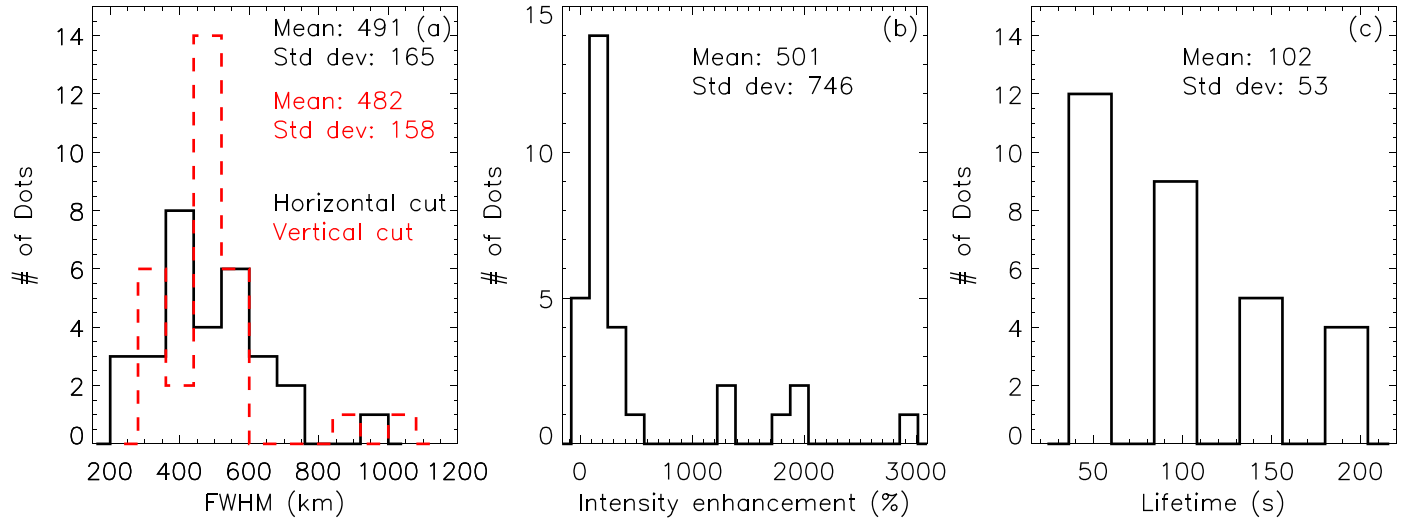

Figure 7. Histograms of the sizes, intensity enhancements, and lifetimes of 30 dots from our Bifrost MHD simulation. Panel (a) shows histograms of the horizontal and vertical sizes of dots. Panel (b) shows the histogram of intensity enhancements with respect to the immediate surroundings of dots. Panel (c) displays the histogram of lifetimes of dots.

3.3.1. Synthetic O V/VI and Si IV Emissions

Although we mainly focus on Fe IX/X intensities for the majority of our analysis, we created images of synthetic O V and O VI emissions, as well as Si IV emissions, to see whether dots are conspicuous in these cooler TR lines. The main reason for synthesizing O V/VI lines is that the EUI HRI_{EUV} 174 Å and SDO/AIA 171 Å passbands do contain O V 172.2 Å and O VI 173 Å lines (e.g., Del Zanna et al. 2011). We averaged O V and O VI emissions to create an O V/VI map, in the same way as done for Fe IX/X emissions.

The O V and O VI lines form at temperatures of 280,000 and 320,000 K, respectively. But the O VI line profile has a very long tail toward higher temperatures, and it is often more coronal-like in its appearance (Dere et al. 1997). Thus, the averaged O V/VI images cover temperatures from about 200,000 K up to a million kelvin. The Si IV line forms in the TR at about 80,000 K. Thus, these lines cover the cooler to hotter TR and lower corona. IRIS SJI 1400 Å images show similar dots in an emerging flux region to that seen in HRI_{EUV} and in the synthetic O V/VI and Si IV images—see an example image from IRIS SJI in 1400 Å in Figure 16. Such bright dots have also been observed in CBPs in Mg II *k* and C II SJIs (Kayshap & Dwivedi 2017). Similar dots have also been observed by Rutten & Rouppe van der Voort (2017) in magnetic network concentrations—there most bright SJI 1400 Å grains coincide with the magnetic concentrations seen in the far wing of Hα. A detailed analysis of the dots in this region of IRIS observations is beyond the scope of the present paper but will be presented in a follow-up study. Figure 17 shows the images in O V/VI and Si IV emissions corresponding to that in Figure 6 for Fe IX/X lines.

To find out whether dots in the simulation are really at mostly MK temperature or at TR temperature, we estimated how bright the O V/VI emission is in the dots relative to the Fe IX/X emission. The ratios O V/VI to Fe IX/X and O V to Fe IX/X for an example dot are shown in Figure 10. The ratio plots (Figures 10(d) and (e)) suggest that the dots have a significant contribution from the TR emission. The dot obviously also has coronal emission. This suggests that dots are multithermal, possibly formed at low heights. Nonetheless, "low height" is only a conjecture because we assume that the TR is under the corona. In reality, TR could just come from the outer part of a feature (like a jet) that is cooler inside, as in Hillier & Arregui (2019).

When we compare the five example dots of Fe IX/X emissions from Figures 8 and 9 with those in O V/VI and Si IV emissions, we can notice that the dots are either bigger, expanded in size (dots 2, 3, and 5) in the TR lines, or extended in one direction along a loop- or jet-like structure (dots 1 and 4). In particular, when one follows their evolution, half of the dots extend as a loop or a surge/jet. This behavior is consistent with flaring arch filaments (FAFs) reported by Vissers et al. (2015). A closer look at AIA 1600 and 1700 Å images does not show enhanced activity associated with dots in Figure 15, thus questioning these dots being related to FAFs. Obviously, this subject requires a further detailed investigation using simultaneous UV and EUV observations.

Further, some dots can be either part of a loop or tiny loops themselves. Most dots in Fe IX/X emission appear to be at the chromospheric/TR base of a loop. We analyze other different properties of the simulated dots in the Fe IX/X, O V/VI, and Si IV emissions. For example, we investigated their Doppler speeds, proper motions, and magnetic field distributions together with their 3D magnetic configurations, given below, which were not possible with the available observations.

3.3.2. Proper Motion of Dots and the Speed of Intensity Propagations in Fe IX/X Emission

We quantified the proper motion and/or intensity propagation of dots. For this purpose, we created time–distance maps along the longer extension of each dot during their evolution. In Figure 11, we show time–distance maps of five example dots (from Figures 8 and 9) to illustrate how the speeds were calculated. For the dots that remain isolated and do not show any extension we only measured their proper motion, if any. Most of the dots move very little themselves, having speeds of $\leqslant 10\,\mathrm{km\,s^{-1}}$, but intensity propagations in them can be as fast as $30\,\mathrm{km\,s^{-1}}$. However, a majority of the dots show a speed of $<10\,\mathrm{km\,s^{-1}}$ in their intensity propagation as well. These speeds are consistent with those in observations (estimated for 20 randomly selected dots). These intensity propagation speeds are on the lower end of those found by Mandal et al. (2021) for brightenings in a quiet solar coronal region and show similarities with loop-like and jet-like fine-scale

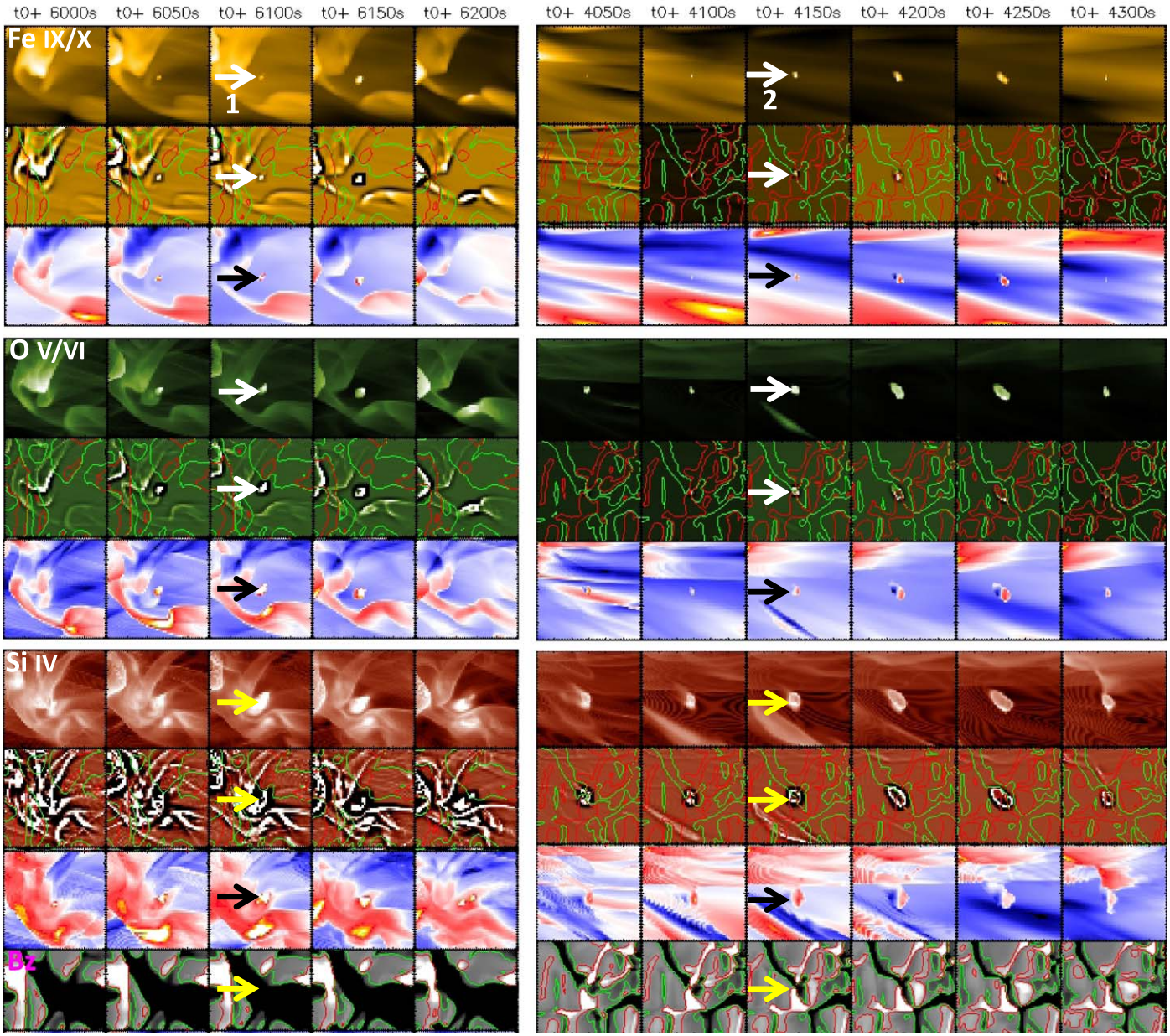

Figure 8. The evolution of two example dots, named 1 and 2, in the synthetic Fe IX/X images. These dots are marked by white (or yellow and black for better visibility) arrows when they are most roundish. The top three rows represent the Fe IX/X intensity image, its unsharp masked image, and the Doppler velocity map, respectively. The same maps for O V/VI and Si IV lines are plotted in the middle and bottom three rows, respectively. There is an additional row at the bottom of the bottom row containing the vertical component of the magnetic field, Bz. The Bz contours (of level ± 20 G) are overplotted on the Bz maps and on the unsharp masked images of Fe IX/X emission. The FOV is ~5 × 5 Mm^2.

explosive events seen by Hi-C 2.1 in an active region (Tiwari et al. 2019).

We note that dot 1 shows back-and-forth motion during its second and third frames (after its 50th second), after showing an initial displacement in the first 50 s. We took the speed along its path of the longest extension. Similarly, dot 3 shows random motion in three directions—first slightly toward north, then toward south, and then toward west. The estimated speed in Figure 11 is when the dot moves toward west because then it showed the most significant displacement. The speeds in the first two steps were each at 2 km s^{-1}. Several other dots show similar back-and-forth or random motion—this could be driven by magnetoacoustic waves from the lower atmosphere.

Dot 5 shows an explosive surge-like behavior with the fastest brightness propagation of the five examples, at a speed of 28 km s^{-1}. Dot 4 also shows a smooth unidirectional plasma flow. There are several of such dots showing unidirectional and several showing bidirectional plasma flow (back and forth, not at the same time) and intensity propagations. This finding is similar to that found in short loops and surges of Hi-C 2.1 observations (Tiwari et al. 2019).

3.3.3. Bifrost Dot Doppler Shifts

The dots in our simulation exhibit distinct Doppler shifts, not only in Fe IX/X emission but also in O V/VI and Si IV emission; see, e.g., qualitative pictures in Figures 8 and 9. In fact, the

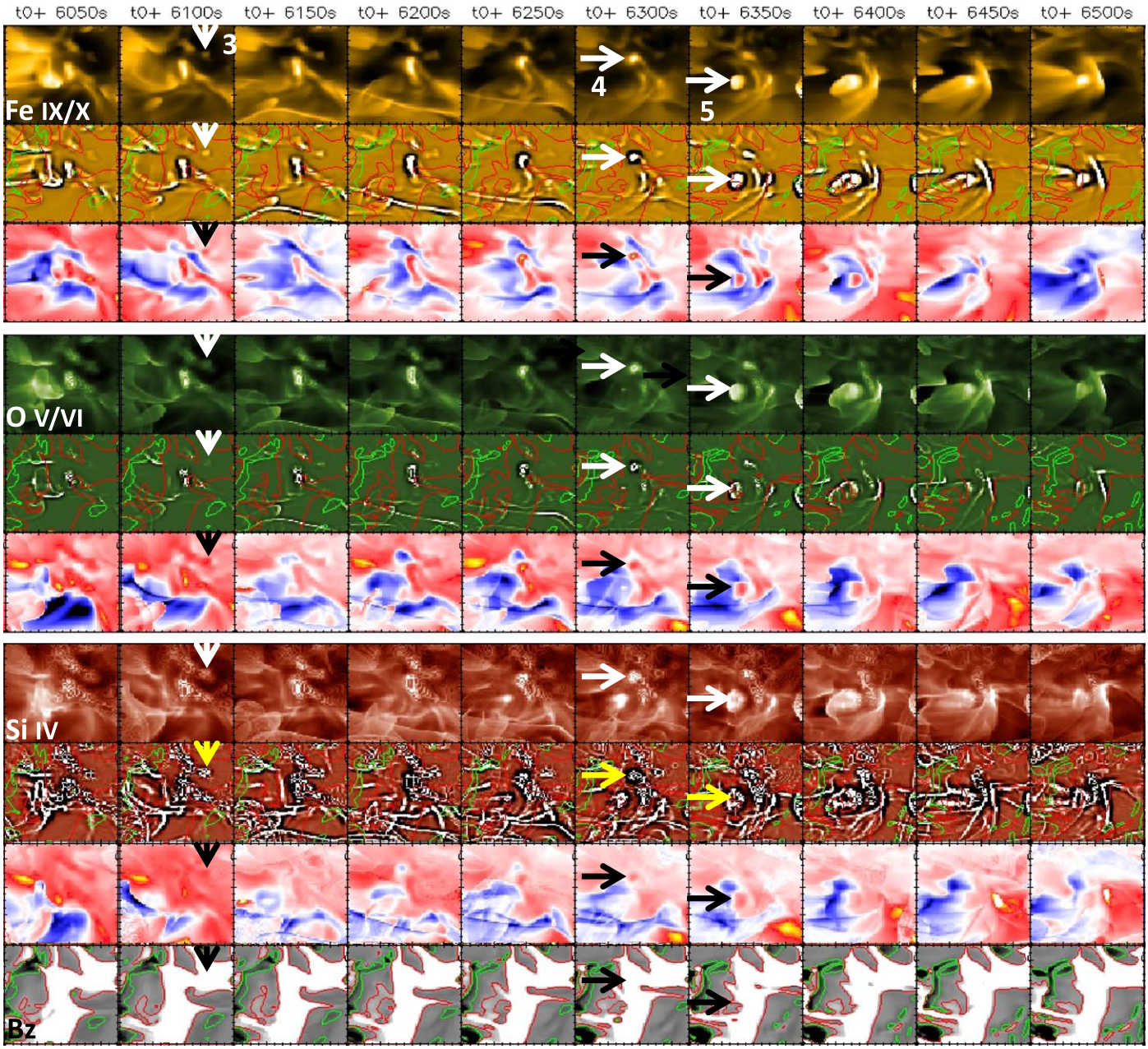

Figure 9. Same as Figure 8, but displaying a different region with three additional examples of dots, namely, 3, 4, and 5.

strength of Doppler speed increases in O V/VI and Si IV lines. Some dots exhibit only redshifts (e.g., dot 1). A few dots in our sample contain only blueshifts in Fe IX/X images (e.g., dot 3). However, more commonly dots exhibit mixed Doppler shifts, i.e., redshift and blueshift next to each other; see, e.g., dots 2 and 5. Also for dot 4, the redshift is surrounded by blueshifts, but blueshifts are not as isolated as in dots 2 and 5. Consistent with their intensity images, Dopplergrams of dots do show an expansion of dots in O V/VI and Si IV lines as compared to their appearance in Fe IX/X lines. The $v_{\rm Dopp}$ maps show extended flows along the dot's longer extension appearing as a loop or a surge/jet.

For a quantitative picture of Doppler flows of dots in Figures 8 and 9 we take a cut along each dot and plot their Doppler speed along it in Figure 12. To follow the plasma flows, we make the plots of Doppler speeds in two consecutive image frames for each dot. Most dots show redshifts either weak or strong up to 75 km s^{-1} in Fe IX/X lines and up to 100 km s^{-1} or more in O V/VI and Si IV lines. The downflows are always stronger in O V/VI and Si IV lines.

3.3.4. Magnetic Field Distribution and Geometry

Consistent with the SDO (AIA+HMI) observations, more than 50% of the dots that we analyze from the simulation have mixed-polarity magnetic flux at their base and have sharp neutral lines, or are at the edges of strong magnetic flux patches. This suggests that magnetic reconnection in the lower atmosphere due to the interaction of lower and higher loops is possible. Once magnetic reconnection happens, the resultant lower loops will submerge into the photosphere displaying magnetic flux cancellation in magnetograms. Magnetic reconnection can happen in between the preexisting and emerging field, or between two existing small loops when the magnetic field gets sheared (as normally visible in Bz maps), creating a

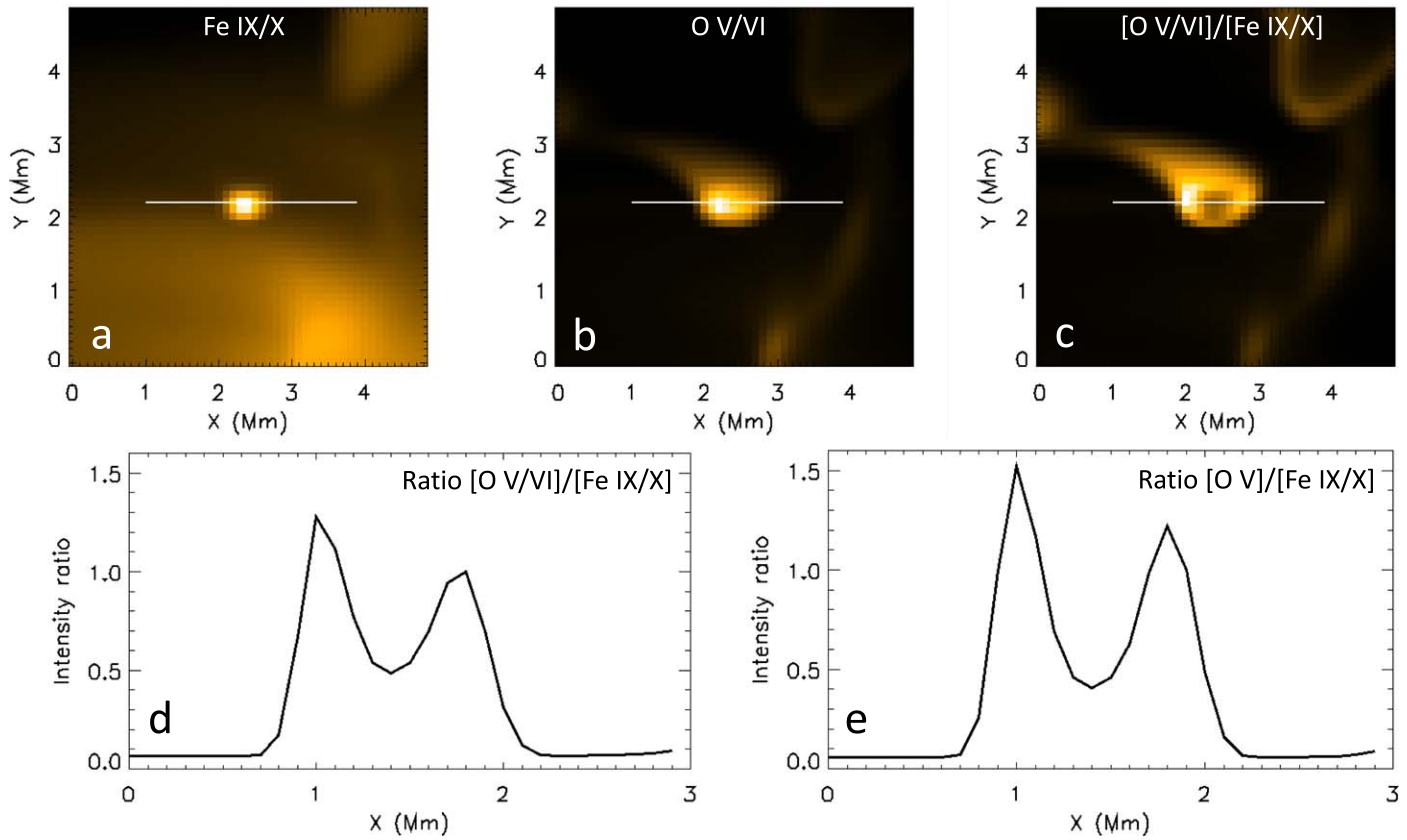

Figure 10. Line ratios of O V/VI to Fe IX/X for a typical dot from the Bifrost MHD simulation. Panels (a) and (b) show the images of the dot in Fe IX/X and O V/VI lines. Panel (c) contains the image of the ratio of O V/VI to Fe IX/X lines. A horizontal line in each panel crosses the dot in the horizontal direction. Panels (d) and (e) show the intensity profiles of the ratios [O V/VI]/[Fe IX/X] and [O V]/[Fe IX/X] along the horizontal line in panel (c). The intensity profiles suggest that the O V/VI lines are equally as strong as the Fe IX/X lines and could play a significant role in the appearance of dots observed with HRI_{EUV}.

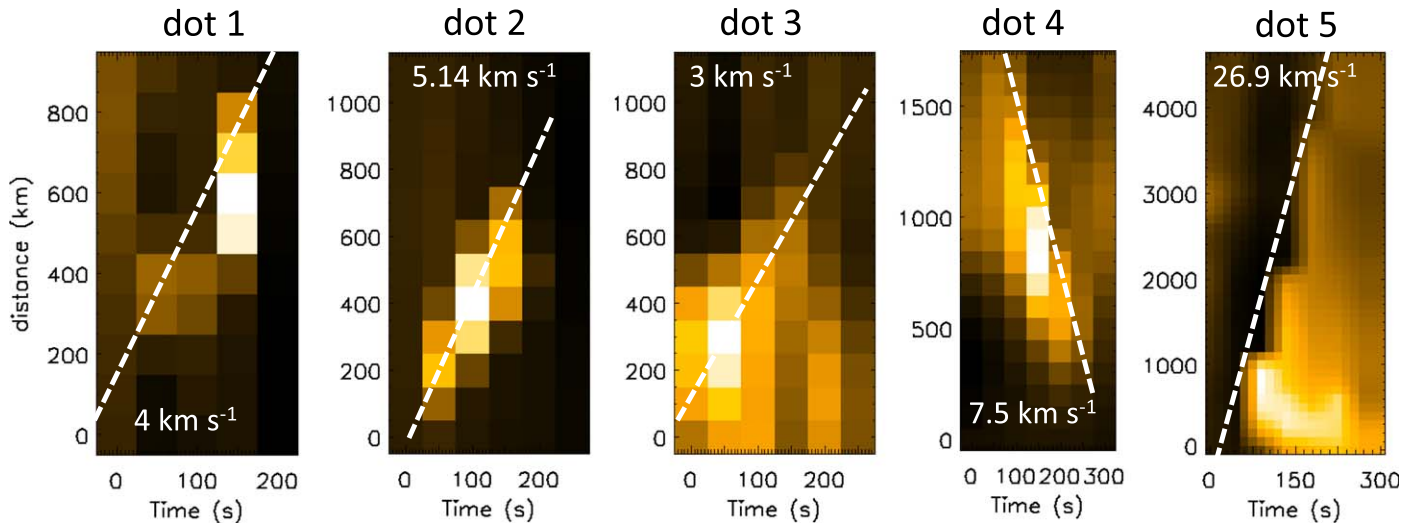

Figure 11. Time–distance maps, along the longer extensions of each of the five example dots from the simulation, to demonstrate how we estimated the brightness propagation speeds of dots. The dashed white line in each panel is to guide the eye along the intensity propagation. The estimated speeds are printed on each map.

suitable magnetic environment for reconnection (e.g., as shown in Figure 14 of Tiwari et al. 2019).

We traced the magnetic field lines near each of the five example dots to verify that the above idea of dot formation is consistent with their field geometry. For this purpose, we used the visualization software tool VAPOR (Li et al. 2019). The magnetic field geometry of five example dots is shown in Figure 13. Red and blue colors in the extrapolated loops correspond to the positive and negative photospheric magnetic field, respectively. Out of our five dots, four (dots 1, 2, 4, 5) show field lines interacting closely, at acute angles, low in the atmosphere (≈1 Mm from the surface), suitable for magnetic reconnection. These locations of interacting field lines are also the locations where the dots are seated, thus suggesting their formation by magnetic reconnection.

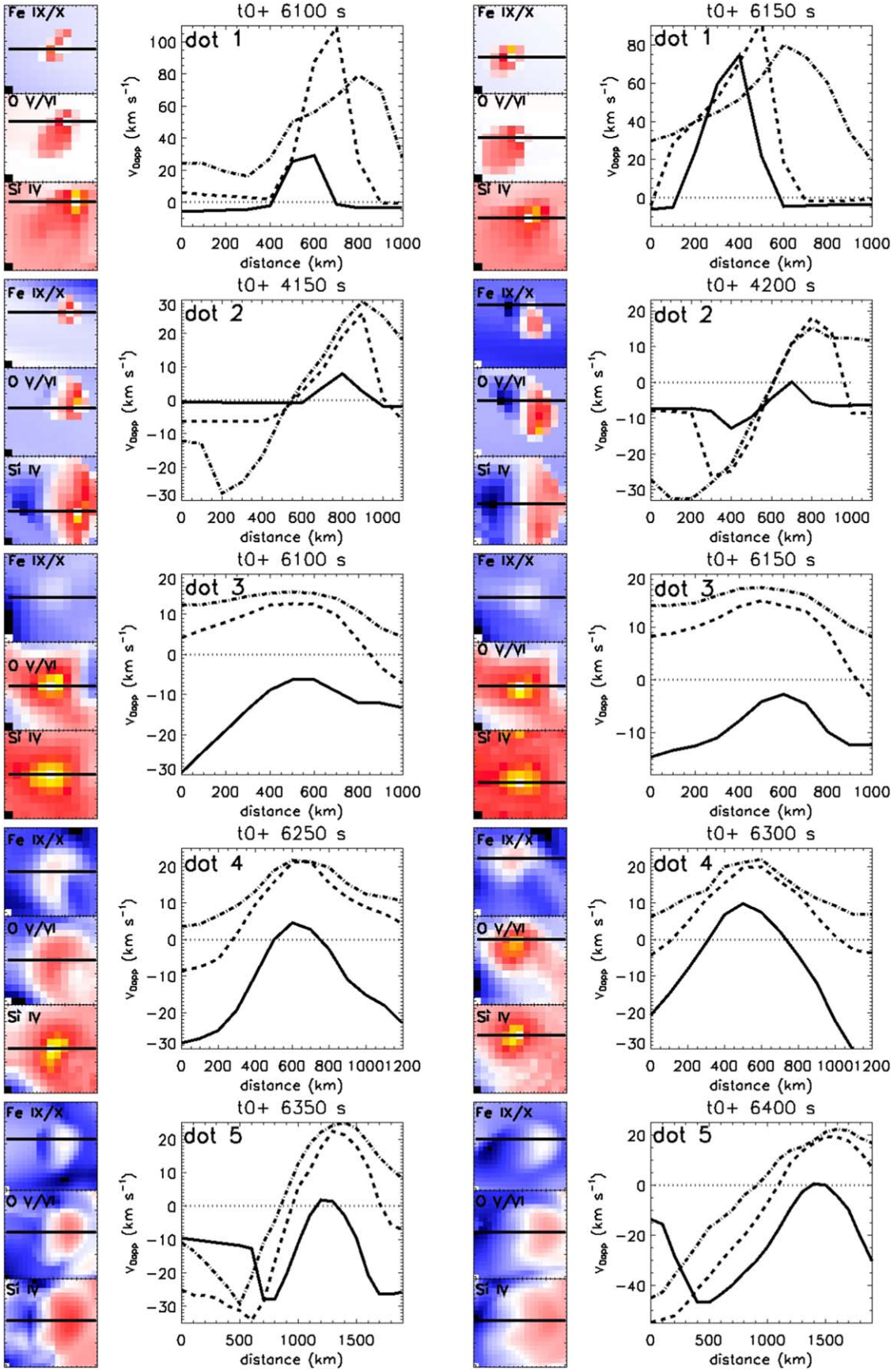

Figure 12. Doppler velocities along a horizontal cut of each of the five example dots shown in Figures 8 and 9. In the images of the Dopplergrams of dots, zero is gray/white, red is downflow, and blue is upflow. For each example dot two consecutive image frames are plotted to show how the dot evolves in the first 50 s. The FOV for each dot is the same in the Dopplergrams of the three spectral lines. The horizontal solid black line on each Dopplergram image marks the cut along which the Doppler speed is plotted on their right. Solid, dashed, and dashed–dotted lines in the plots are for Fe IX/X, O V/VI, and Si IV lines, respectively. A dotted horizontal line in each plot marks the zero velocity level.

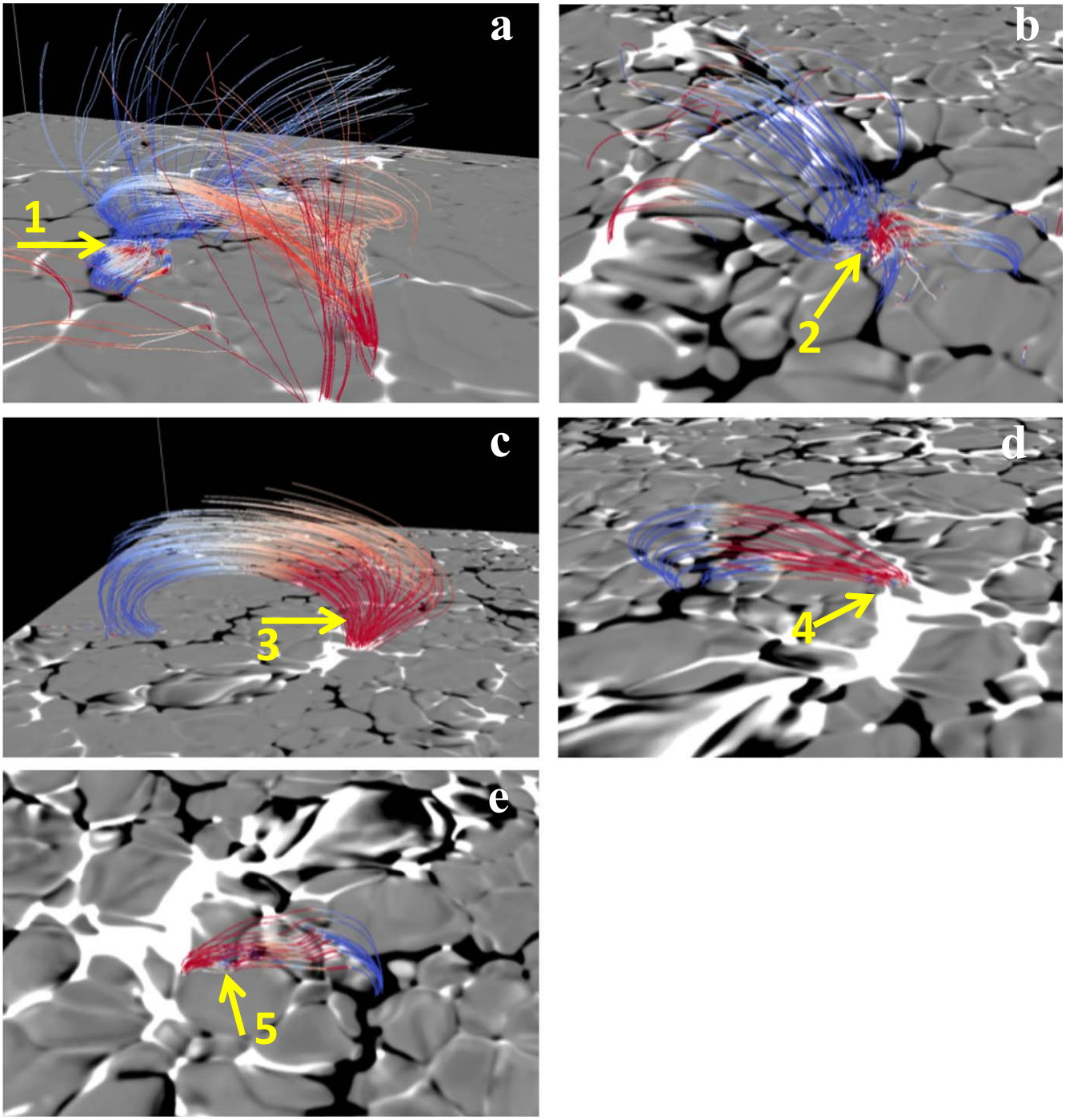

Figure 13. Magnetic field geometry of the five example dots from the simulation. The background images in each panel are Bz maps, saturated at ±500 G. Arrows point to each dot's approximate location. Red and blue colors correspond to positive and negative magnetic fields, respectively. Mixed-polarity magnetic flux is apparently present near four of the five dots (dot 3 is an exception), displaying crossing of the field lines in the lower atmosphere.

One of the dots (dot 3) does not show any tangled magnetic field near its location and thus has a possibility of its origin by waves, or downflows. However, this particular dot does not show downflows in Fe IX/X lines but does show downflows of 10–20 km s^{-1} in O V/VI and Si IV lines (Figure 12). Thus, this dot is more likely formed by magnetoacoustic shocks. We further analyzed this dot in the simulation and found that the dot is indeed formed as a result of magnetoacoustic waves (or shocks). These waves are generated as a result of nearby flux emergence that perturbs the coronal/TR plasma. Thus, although photospheric convection pulls the emerging dipole apart, this dot can more directly be linked to the wave motions produced by the interaction of the overlying magnetic field and the emerging magnetic field as it rapidly expands.

4. Discussion

We have characterized fine-scale dot-like coronal EUV brightenings observed by SolO/EUI HRI_{EUV} in an emerging magnetic flux region. These dots are tiny entities within a classical CBP. We also analyzed simultaneous SDO/AIA and SDO/HMI data and compared observed dots with similar bright dots found in a Bifrost MHD simulation of an emerging

flux region. During their evolution half of the dots either extend, sometimes explosively, to become a loop, or a surge/jet, or result from and at the end of a loop/surge activity. Some of the brighter and bigger dots may be considered as "dot-like" campfires found in the quiet solar regions (Berghmans et al. 2021; Panesar et al. 2021). Thus, different small-scale coronal dynamic features such as loops, surges/jets, campfires, and any other magnetic structures with plasma flows most likely exhibit dot-like brightenings at their base, or sometimes on their bulk/apex, during different evolutionary phases. Half of the dots remain isolated during their lifetime, do not show any extensions, and are not accompanied by any of the above structures (e.g., dot "b" in Figure 2).

Somewhat similar (in sizes and lifetimes) EUV bright dots were observed in an active region (unipolar) plage by Régnier et al. (2014) in 193 Å of Hi-C data (Kobayashi et al. 2014), limited to 5 minutes of observations. They found their EUV dots to be the foot of much longer coronal loops. Most of our dot locations are also at or near the foot of coronal loops, but these loops are relatively "short," being rooted in the initial phase of an emerging bipolar region. Our dots in the emerging flux region are likely a result of magnetic reconnection between the emerging and the preexisting magnetic field. However, a couple of other possibilities, as discussed below, cannot be ruled out. Different dots are consistent with the following three different formation mechanisms.

1. Magnetic reconnection: The SDO observations show that most of the bigger and brighter dots (e.g., dots "a" and "c" in Figure 4) are rooted at strong magnetic field patches, which are often surrounded by opposite-polarity magnetic flux elements, and have sharp PILs. These dots are accompanied by magnetic flux emergence and/or cancellation. Similar to that in observations, in their photospheric magnetograms, many dots in our simulation are located either at a sharp neutral line or at the edge of a strong magnetic flux patch. Further, many dots in the simulation display both redshifts and blueshifts next to each other (see, e.g., dots 2, 4, and 5), consistent with them being a result of magnetic reconnection. Our simulation shows that the magnetic reconnection happens between the emerging and preexisting magnetic field in the lower solar atmosphere at $\approx$1 Mm above the photosphere.

Magnetic reconnection in the lower solar atmosphere results in a shorter loop and a larger loop (Parker 1979; Priest & Forbes 2000). The reconnected-shorter loop submerges into the photosphere if the loop is shorter than a certain length and the magnetic tension dominates over the pressure (van Ballegooijen & Martens 1989; Moore & Roumeliotis 1992; Priest 2014). As a result of the submergence of this short loop into the photosphere, magnetic flux cancellation would be seen (e.g., Tiwari et al. 2014, 2019). However, if the resultant loop is long enough so that magnetic tension loses to magnetic pressure, then the reconnected loop does not submerge into the photosphere, and no flux cancellation would be seen (Priest et al. 1994; Syntelis & Priest 2020).

This magnetic reconnection scenario is well represented in Figure 14 of Tiwari et al. (2019), which also demonstrates why many of the dots appear as an extended loop during their evolution. In the case of the longer dashed loop (in Figure 14 of Tiwari et al. 2019), sometimes only the reconnection site becomes visible as a dot in the corona—the extended dashed loop may remain at much lower TR temperature, as evident in the Bifrost MHD simulation presented here. Thus, dots in Fe IX/X emission are smaller than in cooler (O V/VI and Si IV) lines most likely because only the hottest counterpart of the magnetic reconnection events is visible in the hotter channels. Other parts of the loop reconnection system do not make it to those MK temperatures. The presence of extended structures from dots, during their evolution, further suggests that magnetic reconnection, at the feet of coronal loops (in the chromosphere or TR), is the key cause for generating these dots.

The magnetic reconnection between emerging and preexisting magnetic field, resulting in hot EUV plasma blobs and loops, has also been reported recently by Hou et al. (2021b). Thus, our reconnection idea of dot formation is in general agreement with the scenario of dot formation in Tian et al. (2014b), Alpert et al. (2016), Toriumi et al. (2017), and Tian et al. (2018). This reconnection scenario, in some ways, is also consistent with the formation of other small explosive events, including various chromospheric/TR brightenings and surges/jets (e.g., Gupta & Tripathi 2015; Rouppe van der Voort et al. 2017; Gošić et al. 2018; Panesar et al. 2018a, 2019; Tiwari et al. 2019; Shen et al. 2022).

2. Magnetoacoustic waves: The possibility of some of our dots being generated by magnetoacoustic waves cannot be ruled out. The chromospheric shocks, driven from the photospheric convection, can impact the TR/lower corona along coronal loops. This scenario is similar to that proposed for bright dots observed in the TR by IRIS (Martínez-Sykora et al. 2015; Skogsrud et al. 2016). It is important to note that the EUI 174 Å passband covers O V/VI lines, which form at a much cooler temperature than 1 MK, and supports the idea of some of the HRI_{EUV} dots being at the TR temperature and likely a result of the chromospheric/TR shocks. The line ratios O V/VI to Fe IX/X in our simulation (Figure 10) show that the O V/VI lines are equally as strong as the Fe IX/X lines, suggesting that O V/VI lines could play a significant role in the appearance of the dots observed with HRI_{EUV}, because the wavelength passband is broad and contains all of these lines. Furthermore, the footpoints of hot coronal loops in HRI_{EUV} 174 Å or AIA 171 Å passbands are often formed in the TR, not in the corona (Del Zanna et al. 2011). This possibility is also confirmed by our MHD simulation in a few cases (e.g., dot 3 in Figure 13) where no tangled fields suitable for reconnection are found.

3. Impact of downflows: Bright dots can also be created by the impact of downflows along coronal loops to the higher density of the chromosphere and TR. Thus, there will be an increased local density and temperature caused by the impact of those strong downflows on the higher-density lower atmosphere, by shocks or by collision effects. This scenario is similar to that proposed by Kleint et al. (2014), Tian et al. (2014b), and Alpert et al. (2016) for some of their dots. The loops in the observations of Kleint et al. (2014) were much longer, and the speeds of downflows were supersonic, of the order of 100 km s^{-1}. Some of our dots in the Bifrost MHD simulation do show Doppler speeds of close to 100 km s^{-1} or more, but most of them have a downflow speed of $\leqslant$20 km s^{-1} and are not supersonic, particularly in Fe IX/X emissions. This could be due to either the limited coronal height of loops in the simulation box or the fact that both observations and the simulation contain only smaller loops, with them being in an initial phase of the emergence. This could probably mean that most, if not all, of the dots in the emerging flux region likely have a different formation mechanism than them being a TR/chromospheric response of downflows. Future, simultaneous IRIS and HRI_{EUV} observations of an emerging flux region would help address this subject rigorously.

We further note that the above-mentioned studies (i.e., Kleint et al. 2014; Tian et al. 2014b; Alpert et al. 2016) are focused on the dots in sunspot umbrae and penumbrae, in much stronger

magnetic field regions, and in different magnetic topology than the ones investigated here—those dots may have a completely different origin. The bright coronal dots reported in sunspot penumbrae in 193 Å of Hi-C by Alpert et al. (2016) have similar sizes (~500 km) and horizontal speeds (<10 km s^{-1}) but have much longer lifetimes (270 s) and intensity enhancements (190% from surroundings). Those dots were proposed to form by magnetic reconnection between the two inclined penumbral magnetic field components (penumbral filaments and spines; see, e.g., #7.1 of Hinode Review Team et al. 2019; Tian et al. 2014b; Alpert et al. 2016). The magnetic reconnection scenario proposed for those dots might also work for some of the dots studied here.

Although some of our dots (the larger and brighter ones) match with those reported by Tiwari et al. (2019), in Hi-C 2.1 observations, in that mixed-polarity magnetic flux can be observed at or near the base of dots, Hi-C 2.1 did not show the dots as dim and tiny as observed here. Furthermore, Hi-C 2.1 observations showed much fewer dots than observed in the HRI_{EUV} emerging flux region, probably because the active region was at the peak of its lifetime (as discussed in Tiwari et al. 2021) and most of the global emergence had already stopped in that active region. There might be different reasons for observed differences in the dots in the quiet-Sun emerging flux region versus the dots and tiny loops of Hi-C 2.1 in the core of a mature active region. First of all, there simply is not as much reconnection in a mature active region, with ceased flux emergence, as in the emerging flux region in the quiet Sun. Second, bright surroundings in the active region core might not allow us to detect tiny and rather dim dots in the intensity images. Third, about half of the Hi-C 2.1 images were blurred/smeared owing to pointing instabilities (Rachmeler et al. 2019). Fourth, it is quite possible that such tiny events as covered by EUI/HRI_{EUV} did not occur during the 5-minute Hi-C 2.1 observations (or at least during the good image frames). Moreover, the wavelength band of Hi-C 2.1 was broader (~165–180 Å) than that of EUI (171–178 Å), thus possibly capturing more of chromospheric/TR emission than that of HRI_{EUV}. A caveat for this argument is that there are not many TR lines between 165 and 170 Å.

Previous MHD models have shown that magnetic reconnection between emerging and preexisting magnetic field can result in the formation of surges/jets (Shibata et al. 1992; Yokoyama & Shibata 1995; Moreno-Insertis & Galsgaard 2013; Nóbrega-Siverio et al. 2016). Because our dots are seen in an emerging flux region and show extension, the same mechanism might be at work in dots at much smaller scales—this is what our modeling results consistently suggest (although see, e.g., Panesar et al. 2018b, and references therein, for a different idea for jet formation). As previously mentioned, some of the dots are probably the hottest counterparts of jets/surges or loops.

The dots in our study represent the size of the smallest campfires (Berghmans et al. 2021). Note that the term "campfire" represents different coronal brightening events, such as dots, loops, and jets (Panesar et al. 2021). The dot-like campfires have a size of the order of 1000 km, and they reside above PILs (Panesar et al. 2021). However, the lifetimes and intensity enhancements of dot-like campfires are much larger than those for our dots. Using a triangulation method on simultaneous HRI_{EUV} and SDO/AIA data, Berghmans et al. (2021) and Zhukov et al. (2021) found that the height of most campfires from the photosphere is ⩽5 Mm. Chen et al. (2021) proposed, based on their MHD simulation, that component magnetic reconnection generates the largest of campfires, the reconnection taking place at the apex of loops, higher in the corona between 2 and 5 Mm from the photosphere. Most dots in our simulation show extension as a loop or jet in O V/VI and Si IV lines, and the brightest part appears as a dot in the Fe IX/X lines—this suggests that for dots the reconnection takes place in the lower atmosphere near the TR/chromospheric footpoint of the loop, where flux emergence occurs and the short emerging loop reconnects with the existing (already emerged) loop. The geometrical configuration of dots in our simulation consistently shows the interaction of short and long loops at a height of ≈1 Mm from the photosphere. Thus, some of the properties of campfires are similar to the fine-scale dots investigated here, except that our dots form much lower in the atmosphere, at ≈1 Mm from the photosphere.

Thus, our findings also suggest that the heating might not always start from magnetic buildup and triggering at the apex of loops but might often begin at their footpoints, low in the corona/TR/chromosphere.

The extension of dots, in both observations and simulation, often appears as a propagation of intensity along a loop, or a small-scale jet at a speed of 30 km s^{-1} or less. Note that these intensity propagations are still at much smaller spatial and temporal scales than the smallest coronal jets or jetlets reported in the literature (Raouafi & Stenborg 2014; Tian et al. 2014a; Panesar et al. 2018a, 2019, 2020, 2021; Chitta et al. 2021; Hou et al. 2021a).

Because the majority of our HRI_{EUV} dots in the emerging flux region show coronal (as well as TR) temperatures, the presented dots in this study are not Ellerman bombs (EBs; Ellerman 1917; Rutten et al. 2013). The dots do not show stationary dot-like brightening in AIA 1700 Å either, as noted for EBs (Vissers et al. 2019). However, some of these could be FAFs (Vissers et al. 2015). Some of the dots could also be similar to IRIS bombs (Peter et al. 2014) or UV bursts (Young et al. 2018; Hansteen et al. 2017), but a more extensive investigation is required to settle this issue (Hansteen et al. 2019). Again, note that most of our dots have much shorter lifetimes than UV bursts or IRIS bombs (~5 minutes); see, e.g., Watanabe et al. (2011). Our dots are fine-scale substructures inside a classical CBP and thus obviously are much dimmer, shorter, and smaller than X-ray/coronal bright points (e.g., Golub et al. 1974; Berghmans et al. 2001; Madjarska 2019).

It is more likely that dots observed in different UV and EUV wavelengths in different solar environments are generated in many different ways. This discussion is perhaps analogous to the discussion of the nature of solar EUV blinkers (Harrison 1997; Brković et al. 2001). The appearance of IRIS TR images at much higher resolution suggests that when we observe a variety of features driven by very different physical mechanisms we end up with dots, or similar roundish features when seen with the instruments that observe at a much lower spatial resolution.

Depending on whether a dot has cooler surroundings (i.e., it is isolated), some dots were disregarded owing to not showing 2σ intensity enhancement, which is our selection criterion. This means that there might be many more (dimmer) dots than we consider in the EUI images of the emerging flux region. This can be verified, again, with future coordinated observations of HRI_{EUV} with IRIS.

Assuming a spherical geometry of dots with an average diameter of 650 km and field strength of 200 G (as found in our simulation), the estimated magnetic energy ($B^2 \times V / 8\pi$) of dots comes out to be 2.3×10^{26} erg. Thus, approximate free energy would be in the order of 10^{26} erg (80% of total magnetic energy), which is on the higher side of that of nanoflares (Parker 1988).

This is similar to the energy estimated for EUV dots in a plage region (Régnier et al. 2014), for nanoflares in small loops (Winebarger et al. 2013; Testa et al. 2013), and for smaller campfires (Panesar et al. 2021). Thus, our dot-like events have energies capable of heating the corona to a million degrees, locally. CBPs are believed to be major contributors to the quiet corona, and these dots mark where exactly the heating happens within CBPs. Further elucidation of fine-scale dots within CBPs in the context of quiet-Sun coronal heating is obviously of interest.

The EUI/HRI_{EUV} has opened a new opportunity to better understand fine-scale coronal explosive events. As SolO gets closer to the Sun, better spatial resolution data would be acquired, and co-observations with IRIS will be extremely valuable for such investigations as performed here. Thus, in future spectral data such as those obtained with IRIS and Hinode/EIS, simultaneous to EUI observations, and high-quality magnetograms such as those obtained with Hinode (SOT/SP), SolO/PHI, and DKIST would provide further insights into the formation of SolO's EUI/HRI_{EUV} dots reported here. Of particular interest would be assessing Doppler speeds of dots in different atmospheric heights using IRIS spectra and comparing those with that of Bifrost MHD simulations. Furthermore, sophisticated techniques, such as those presented by Humphries & Morgan (2021) for automatically selecting and characterizing a large number of brightenings, should be used in the future on a much larger sample of dots to assess their common characteristics and corroborate our findings.

5. Conclusions

Using SolO's EUI/HRI_{EUV} 174 Å data, we report on the ubiquitous presence of dot-like fine-scale heating events in and around an emerging flux region. These dots are fine-scale brightening events inside a CBP and contribute to at least some of their heating. The dots are dim ($30\% \pm 10\%$ brighter than their immediate surroundings), small in size (675 ± 300 km), and short-lived (50 ± 35 s), and half of them can be linked to a loop or jet activity of longer span and size. Most of the bigger and brighter EUV dots have a temperature of 1–2 MK, as estimated via DEM analysis of different SDO/AIA passbands, but some are much cooler and might remain at TR/chromospheric temperatures. The line ratios of O V/VI to Fe IX/X for dots in our simulation suggest that the O V/VI lines are equally as strong as the Fe IX/X lines. This indicates that O V/VI lines could play a significant role in the appearance of the dots observed with HRI_{EUV}–as the HRI_{EUV} passband is broad, containing all of these lines.

Many of the HRI_{EUV} dots observed in the emerging flux region are probably the hottest counterparts of TR/chromospheric activities, caused by magnetic reconnection. The Bifrost MHD simulation of a bipolar flux emergence shows that dots have a bigger extension in TR, cooler lines, such as O V/VI and Si IV. Thus, the reconnection site (at ≈1 Mm from the photosphere) getting hot to MK plasma shows up in Fe IX/X emission as a dot-like bright transient event. These contain proper motions of <10 km s^{-1}, but the intensity propagation along their longer extension, when they extend as a loop or surge/jet, can have a speed of up to 30 km s^{-1}. Dots in the simulation often contain mixed Doppler signals in Fe IX/X emission, both blueshifts and redshifts of the order of 10 km s^{-1}, but Doppler speeds can be multiple times larger. Redshifts are always stronger in O V/VI and Si IV lines than in Fe IX/X lines. The magnetic field geometry of dots in our simulation suggests that most dots are caused by magnetic reconnection between emerging and preexisting magnetic field—thus also suggesting that heating in a loop does not always start at the loop's apex, but rather can often start near their TR/chromospheric feet. Thus, our observational and modeling results suggest that magnetic reconnection in these dots plays an important role in some of the coronal heating of emerging flux regions and provides new insights into the heating at fine scales by magnetic reconnection.

Because magnetic reconnection happens low in the TR/chromosphere, the presence of mixed-polarity magnetic flux, as well as flux cancellation due to the submergence of the lower reconnected loops, is consistent with the findings of Tiwari et al. (2019) for dot-like, loop-like, and surge-like events in the core of the Hi-C 2.1 active region and those of Panesar et al. (2021) for dot-like, loop-like, complex, and jet-like campfires in the quiet solar corona. Some dots could well be caused by chromospheric shocks, either directly driven from the photospheric convection or generated from the interaction of emerging and overlying fields. A small percentage of dots could also be a response of the impact of downflows along coronal loops on the TR/chromospheric density. For this, a further detailed investigation is required.

The spatio-temporal filling factor of these dots has yet to be determined. Further, dots found in different magnetic environments and regions in the solar atmosphere may have different formation mechanisms. Whether EUV dots are limited to strong field loops such as those found in plage areas (Régnier et al. 2014), sunspots (Tian et al. 2014b; Kleint et al. 2014; Alpert et al. 2016; Deng et al. 2016), cores of ARs (Tiwari et al. 2019), and emerging flux regions (this work), or are present at the base of each coronal loop even in the weaker magnetic regions, such as in the quiet Sun and coronal holes, as well as in other solar features such as filaments and plumes, remains to be seen.

We would like to thank the referee for carefully reading our manuscript and for constructive suggestions. We thank Mark Cheung (LMSAL) for discussions about DEM analysis. S.K.T. gratefully acknowledges support by NASA HGI award (80NSSC21K0520) and NASA contract NNM07AA01C (Hinode). V.H.H. is supported by NASA grant 80NSSC 20K1272: Flux emergence and the structure, dynamics, and energetics of the solar atmosphere. B.D.P. was supported by NASA contract NNG09FA40C (IRIS). N.K.P.'s research was supported by NASA grant NNG04EA00C (SDO/AIA) and HGI award (80NSSC20K0720). Solar Orbiter is a space mission of international collaboration between ESA and NASA, operated by ESA. The EUI instrument was built by CSL, IAS, MPS, MSSL/UCL, PMOD/WRC, ROB, and LCF/IO with funding from the Belgian Federal Science Policy Office (BELSPO/PRODEX PEA 4000112292); the Centre National d'Etudes Spatiales (CNES); the UK Space Agency (UKSA); the Bundesministerium für Wirtschaft und Energie (BMWi) through the Deutsches Zentrum für Luft- und Raumfahrt (DLR); and the Swiss Space Office (SSO). IRIS is a NASA small explorer mission developed and operated by LMSAL with mission operations executed at NASA Ames Research Center and major contributions to downlink communications funded by ESA and the Norwegian Space Centre. The AIA and HMI data are courtesy of NASA/SDO and the AIA and HMI science teams. We acknowledge imagery produced by VAPOR (www.vapor.ucar.edu), a product of the Computational Information Systems Laboratory at the National Center for Atmospheric Research. This research has made use of NASA's Astrophysics Data System and of the IDL SolarSoft package.

Appendix A
Further Examples of Dots in the HRI_{EUV} Observations of an Emerging Flux Region

In Figure 14 we show two additional image frames from the Figure 2 animation with many dots outlined by yellow boxes.

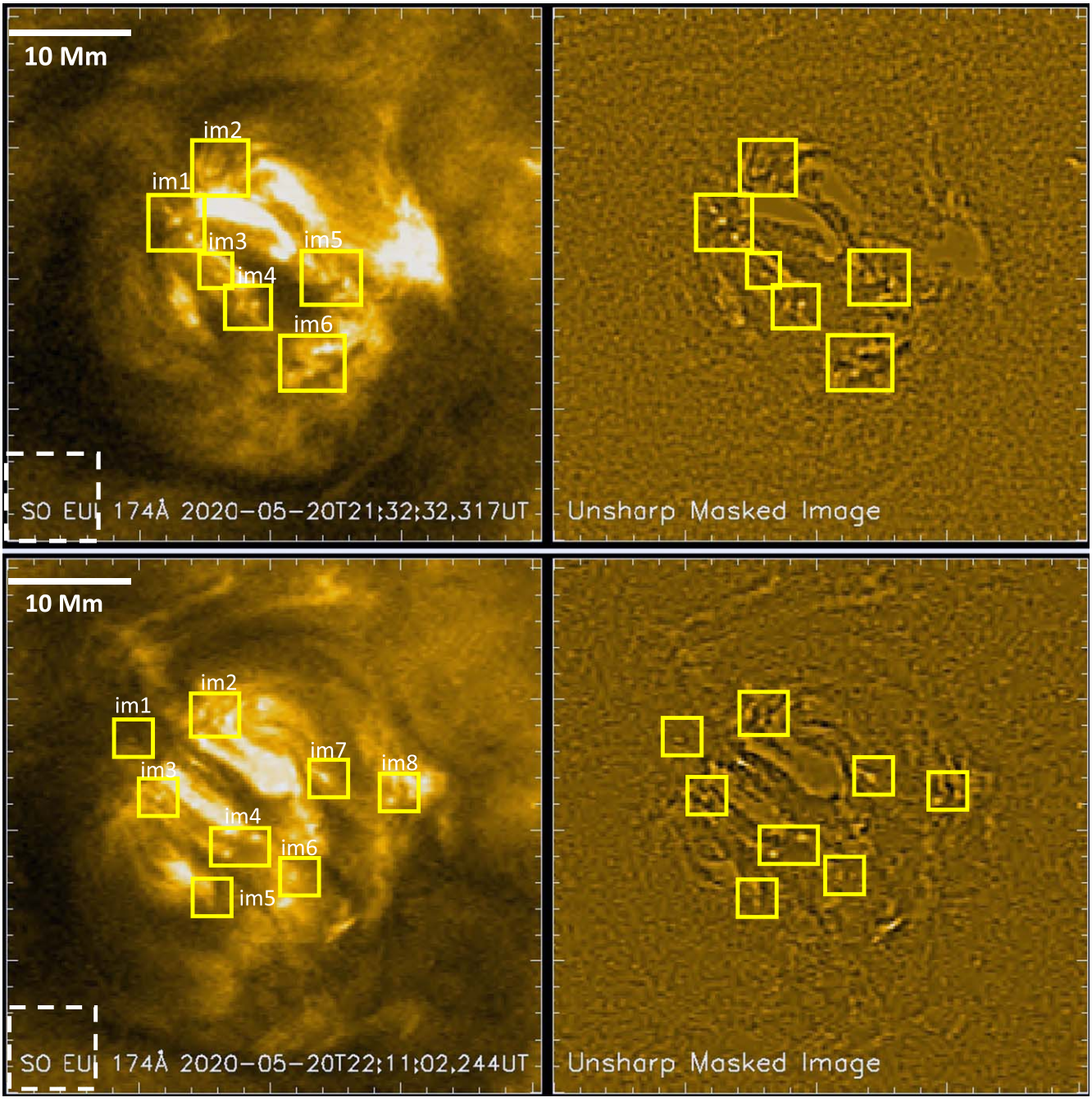

Figure 14. Additional examples of dots in EUI/HRI_{EUV} observations. The left panel in each row is the HRI_{EUV} 174 Å image, and the right panel is the unsharp masked image of it. Different boxes outline the regions of selected dots in each image frame. A white dashed box in the lower left corner of the left panel outlines the region that is used for noise estimation. A white horizontal bar on the 174 Å image scales 10 Mm distance, for reference.

Appendix B
SDO/AIA Images, Corresponding to Figure 4, in Different AIA Channels

Here we show images in different AIA channels of the same time and FOV as shown in Figure 4 for 171 Å. The three dots show faint signatures in the AIA 304, 193, and 131 Å images but are not evident in the AIA 1600, 1700, and 94 Å images.

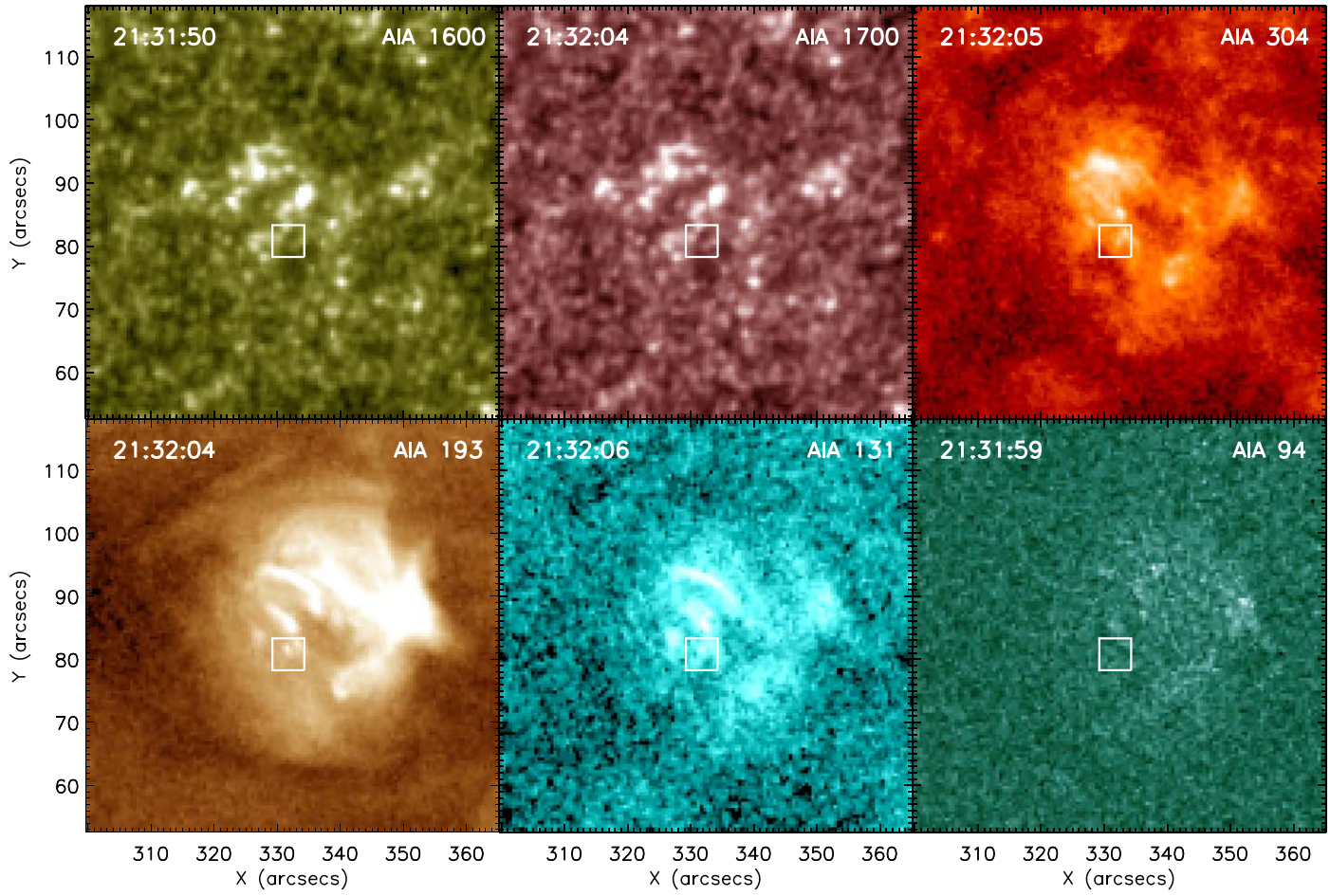

Figure 15. Images corresponding to Figure 4, in different AIA channels. From left to right, AIA 1600, 1700, and 304 Å in the top row, and AIA 193, 131, and 94 Å in the bottom row. A white box in each image is the same as that in Figure 4. Note that, similar to those in Figure 4, these AIA images are de-rotated to the central image time, which is at 2020 May 20 21:44:51 UT. A roll angle correction of 6° is made to match that with HRI_{EUV}.

Appendix C
Dots in IRIS Observations of an Emerging Flux Region

We note that there were no IRIS co-observations with the EUI/HRI_{EUV} data used in the present work. We looked for independent IRIS observations capturing initial phases of magnetic flux emergence, to see whether there are fine-scale dots in these observations of TR/chromospheric lines.

Here we show an example map from IRIS Si IV 1400 Å SJI observations of an emerging flux region, with some dots outlined inside a few boxes on it. The unsharp masked image and corresponding SDO/HMI LOS magnetograms are also displayed.

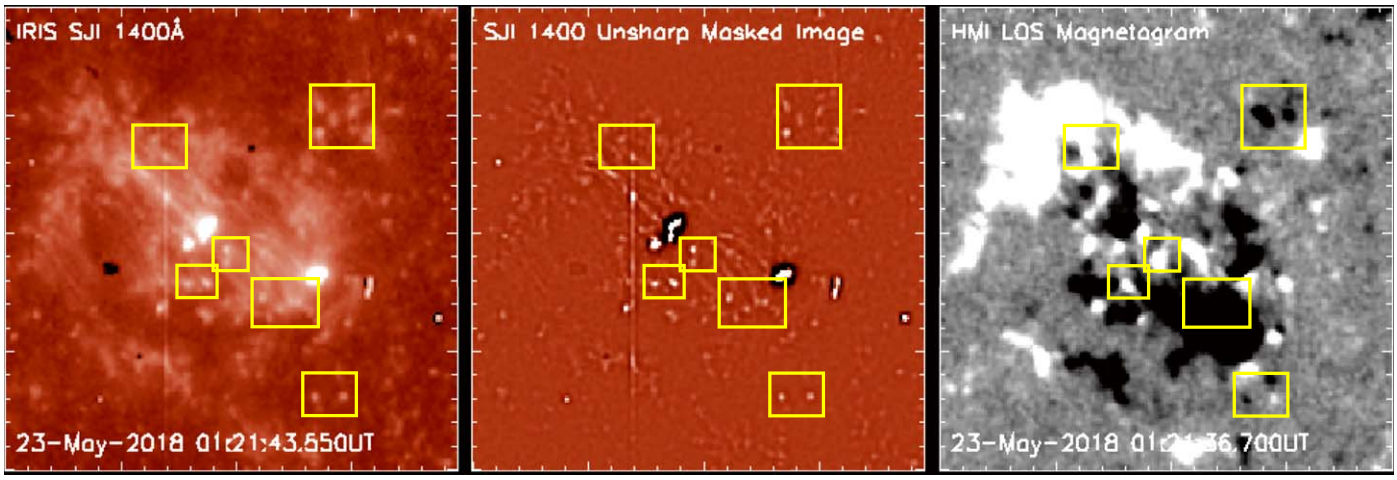

Figure 16. IRIS SJI 1400 Å image (left panel) and its unsharp masked image (middle panel) of an emerging flux region, displayed together with the SDO/HMI LOS magnetogram (right panel) that is the closest in time to the SJI 1400 Å image. Many small-scale dots can be noticed, some outlined by yellow boxes for easy identification. The presence of dots in Si IV lines similar to that of EUI suggests that they could be formed in the TR. However, a detailed study comparing dots one-to-one in the TR and corona will be required to confirm this.

Appendix D
Bifrost MHD Simulation: Synthetic O V/VI and Si IV Lines

Here we plot O V/VI λ172/λ173 and Si IV λ1393 images of the corresponding Fe IX/X image frame shown in Figure 6.

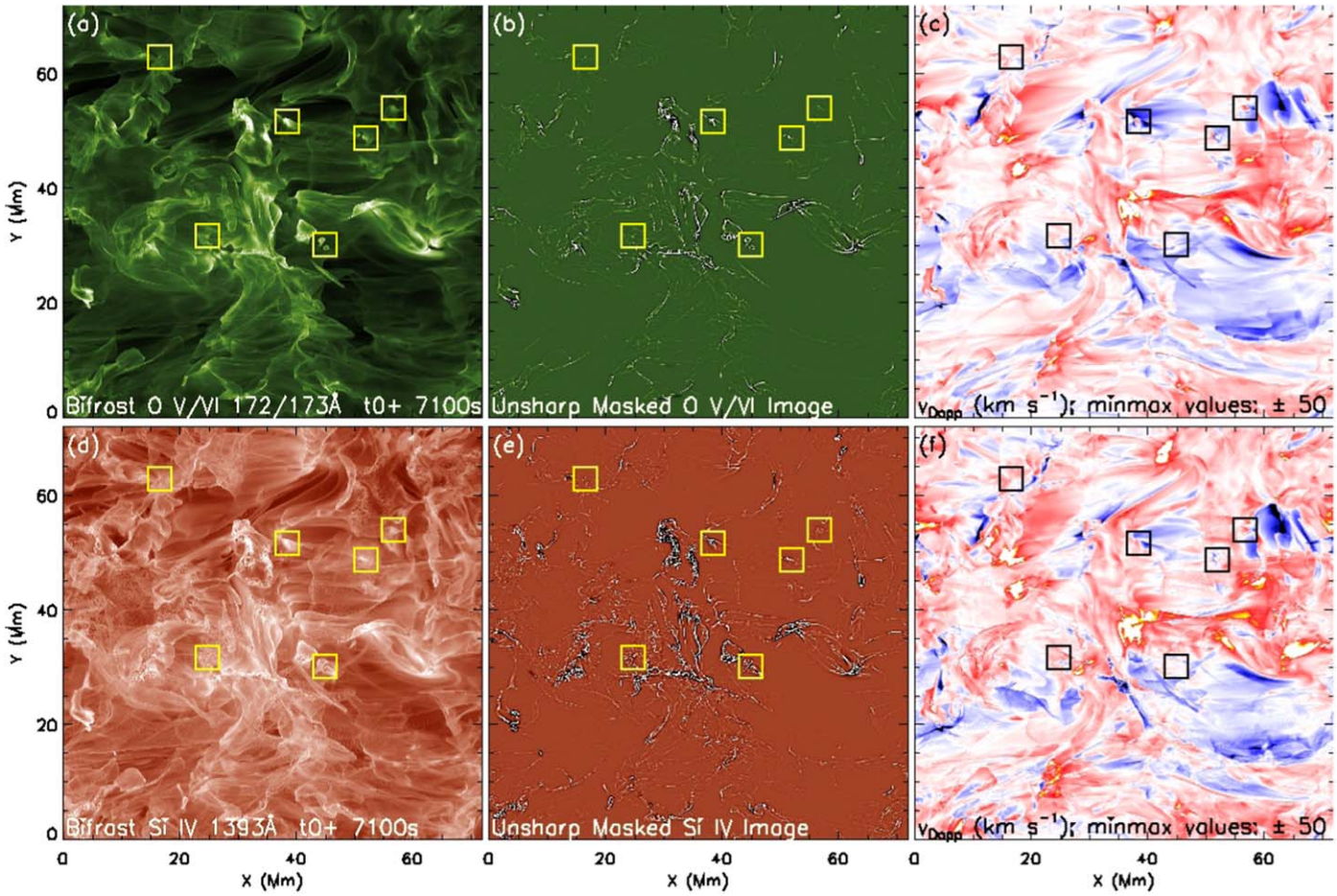

Figure 17. Example image frame (same as in Figure 6 for Fe IX/X lines) of O V/VI and Si IV lines. The dot locations outlined by the yellow boxes are the same as in Figure 6.

ORCID iDs

Sanjiv K. Tiwari https://orcid.org/0000-0001-7817-2978
Viggo H. Hansteen https://orcid.org/0000-0003-0975-6659
Bart De Pontieu https://orcid.org/0000-0002-8370-952X
Navdeep K. Panesar https://orcid.org/0000-0001-7620-362X
David Berghmans https://orcid.org/0000-0003-4052-9462

References

Alpert, S. E., Tiwari, S. K., Moore, R. L., Winebarger, A. R., & Savage, S. L. 2016, ApJ, 822, 35
Archontis, V., Moreno-Insertis, F., Galsgaard, K., Hood, A., & O'Shea, E. 2004, A&A, 426, 1047
Aschwanden, M. J. 2002, SSRv, 101, 1
Aschwanden, M. J. 2004, Physics of the Solar Corona. An Introduction (Chichester: Praxis Publishing Ltd)
Benz, A. O. 2017, LRSP, 14, 2
Berghmans, D., Auchère, F., Long, D. M., et al. 2021, A&A, 656, L4
Berghmans, D., McKenzie, D., & Clette, F. 2001, A&A, 369, 291
Brković, A., Solanki, S. K., & Rüedi, I. 2001, A&A, 373, 1056
Bryans, P., McIntosh, S. W., De Moortel, I., & De Pontieu, B. 2016, ApJL, 829, L18
Carlsson, M., & Leenaarts, J. 2012, A&A, 539, A39
Chen, Y., Przybylski, D., Peter, H., et al. 2021, A&A, 656, L7
Cheung, M. C. M., Boerner, P., Schrijver, C. J., et al. 2015, ApJ, 807, 143
Cheung, M. C. M., & Isobe, H. 2014, LRSP, 11, 3
Chitta, L. P., Solanki, S. K., Peter, H., et al. 2021, A&A, 656, L13
De Pontieu, B., De Moortel, I., Martinez-Sykora, J., & McIntosh, S. W. 2017, ApJL, 845, L18
De Pontieu, B., Hansteen, V. H., McIntosh, S. W., & Patsourakos, S. 2009, ApJ, 702, 1016
De Pontieu, B., Hansteen, V. H., Rouppe van der Voort, L., van Noort, M., & Carlsson, M. 2007, ApJ, 655, 624
De Pontieu, B., Title, A. M., Lemen, J. R., et al. 2014, SoPh, 289, 2733
Del Zanna, G., O'Dwyer, B., & Mason, H. E. 2011, A&A, 535, A46
Deng, N., Yurchyshyn, V., Tian, H., et al. 2016, ApJ, 829, 103
Dere, K. P., Landi, E., Mason, H. E., Monsignori Fossi, B. C., & Young, P. R. 1997, A&AS, 125, 149
Ellerman, F. 1917, ApJ, 46, 298
Falconer, D. A., Moore, R. L., Porter, J. G., & Hathaway, D. H. 1998, ApJ, 501, 386
Falconer, D. A., Tiwari, S. K., Moore, R. L., & Khazanov, I. 2016, ApJL, 833, L31
Fletcher, L., Dennis, B. R., Hudson, H. S., et al. 2011, SSRv, 159, 19
Freeland, S. L., & Handy, B. N. 1998, SoPh, 182, 497
Golub, L., Deluca, E., Austin, G., et al. 2007, SoPh, 243, 63
Golub, L., Krieger, A. S., Harvey, J. W., & Vaiana, G. S. 1977, SoPh, 53, 111
Golub, L., Krieger, A. S., Silk, J. K., Timothy, A. F., & Vaiana, G. S. 1974, ApJL, 189, L93

Gošić, M., de la Cruz Rodríguez, J., De Pontieu, B., et al. 2018, ApJ, 857, 48
Gudiksen, B. V., Carlsson, M., Hansteen, V. H., et al. 2011, A&A, 531, A154
Gupta, G. R., & Tripathi, D. 2015, ApJ, 809, 82
Hagenaar, H. J. 2001, ApJ, 555, 448
Hansteen, V., Ortiz, A., Archontis, V., et al. 2019, A&A, 626, A33
Hansteen, V. H., Archontis, V., Pereira, T. M. D., et al. 2017, ApJ, 839, 22
Harrison, R. A. 1997, SoPh, 175, 467
Harvey, K. L., & Martin, S. F. 1973, SoPh, 32, 389
Hayek, W., Asplund, M., Carlsson, M., et al. 2010, A&A, 517, A49
Hillier, A., & Arregui, I. 2019, ApJ, 885, 101
Hinode Review Team, Al-Janabi, K., Antolin, P., et al. 2019, PASJ, 71, R1
Hou, Z., Tian, H., Berghmans, D., et al. 2021a, ApJL, 918, L20
Hou, Z., Tian, H., Chen, H., et al. 2021b, ApJ, 915, 39
Hudson, H. S. 1991, SoPh, 133, 357
Humphries, L. D., & Morgan, H. 2021, ApJ, 922, 226
Kayshap, P., & Dwivedi, B. N. 2017, SoPh, 292, 108
Kleint, L., Antolin, P., Tian, H., et al. 2014, ApJL, 789, L42
Kobayashi, K., Cirtain, J., Winebarger, A. R., et al. 2014, SoPh, 289, 4393
Kontogiannis, I., Tsiropoula, G., Tziotziou, K., et al. 2020, A&A, 633, A67
Kraaikamp, E., Gissot, S., Auchere, F., et al. 2021, SolO/EUI Data Release, v2.0, Royal Observatory of Belgium, doi:10.24414/z2hf-b008
Lemen, J. R., Title, A. M., Akin, D. J., et al. 2012, SoPh, 275, 17
Li, S., Jaroszynski, S., Pearse, S., Orf, L., & Clyne, J. 2019, Atmos, 10, 488
Longcope, D. W., & Kankelborg, C. C. 1999, ApJ, 524, 483
Madjarska, M. S. 2019, LRSP, 16, 2
Mandal, S., Peter, H., Pradeep Chitta, L., et al. 2021, A&A, 656, L16
Martínez-Sykora, J., Rouppe van der Voort, L., Carlsson, M., et al. 2015, ApJ, 803, 44
Masuda, S., Kosugi, T., Hara, H., Tsuneta, S., & Ogawara, Y. 1994, Natur, 371, 495
Moore, R. L., Panesar, N. K., Sterling, A. C., & Tiwari, S. K. 2022, arXiv:2203.13287
Moore, R. L., & Roumeliotis, G. 1992, in Eruptive Solar Flares. Proc. of Coll. 133 of the IAU, ed. Z. Svestka, B. V. Jackson, & M. E. Machado (New York: Springer), 69
Moore, R. L., Sterling, A. C., Hudson, H. S., & Lemen, J. R. 2001, ApJ, 552, 833
Moreno-Insertis, F., & Galsgaard, K. 2013, ApJ, 771, 20
Müller, D., St., Cyr, O. C., Zouganelis, I., et al. 2020, A&A, 642, A1
Nóbrega-Siverio, D., Moreno-Insertis, F., & Martínez-Sykora, J. 2016, ApJ, 822, 18
Panesar, N. K., Sterling, A. C., Moore, R. L., et al. 2018a, ApJL, 868, L27
Panesar, N. K., Sterling, A. C., & Moore, R. L. 2018b, ApJ, 853, 189
Panesar, N. K., Sterling, A. C., Moore, R. L., et al. 2019, ApJL, 887, L8
Panesar, N. K., Tiwari, S. K., Berghmans, D., et al. 2021, ApJL, 921, L20
Panesar, N. K., Tiwari, S. K., Moore, R. L., & Sterling, A. C. 2020, ApJL, 897, L2
Parker, E. N. 1979, Cosmical Magnetic Fields: Their Origin and Their Activity (New York: Oxford Univ. Press), 1979
Parker, E. N. 1988, ApJ, 330, 474
Pesnell, W. D., Thompson, B. J., & Chamberlin, P. C. 2012, SoPh, 275, 3
Peter, H., Tian, H., Curdt, W., et al. 2014, Sci, 346, 1255726
Polito, V., Testa, P., Allred, J., et al. 2018, ApJ, 856, 178
Priest, E. 2014, Magnetohydrodynamics of the Sun (Cambridge: Cambridge Univ. Press)
Priest, E., & Forbes, T. 2000, Magnetic Reconnection (New York: Cambridge Univ. Press)
Priest, E. R., Parnell, C. E., & Martin, S. F. 1994, ApJ, 427, 459
Rachmeler, L. A., Winebarger, A. R., Savage, S. L., et al. 2019, SoPh, 294, 174
Raouafi, N.-E., & Stenborg, G. 2014, ApJ, 787, 118
Régnier, S., Alexander, C. E., Walsh, R. W., et al. 2014, ApJ, 784, 134
Rochus, P., Auchère, F., Berghmans, D., et al. 2020, A&A, 642, A8
Rouppe van der Voort, L., De Pontieu, B., Scharmer, G. B., et al. 2017, ApJL, 851, L6
Rouppe van der Voort, L. H. M., Joshi, J., Henriques, V. M. J., & Bose, S. 2021, A&A, 648, A54
Rutten, R. J. 2020, arXiv:2009.00376
Rutten, R. J., & Rouppe van der Voort, L. H. M. 2017, A&A, 597, A138
Rutten, R. J., Vissers, G. J. M., Rouppe van der Voort, L. H. M., Sütterlin, P., & Vitas, N. 2013, JPhCS, 440, 012007
Samanta, T., Tian, H., Banerjee, D., & Schanche, N. 2017, ApJL, 835, L19
Scherrer, P. H., Schou, J., Bush, R. I., et al. 2012, SoPh, 275, 207
Schou, J., Scherrer, P. H., Bush, R. I., et al. 2012, SoPh, 275, 229
Shen, J., Xu, Z., Li, J., & Ji, H. 2022, ApJ, 925, 46
Shibata, K., Nozawa, S., & Matsumoto, R. 1992, PASJ, 44, 265
Skartlien, R. 2000, ApJ, 536, 465
Skogsrud, H., Rouppe van der Voort, L., & De Pontieu, B. 2016, ApJ, 817, 124
Svestka, Z. 1976, Solar Flares (Berlin: Springer),
Syntelis, P., & Priest, E. R. 2020, ApJ, 891, 52
Testa, P., De Pontieu, B., Allred, J., et al. 2014, Sci, 346, 1255724
Testa, P., De Pontieu, B., Martínez-Sykora, J., et al. 2013, ApJL, 770, L1
Testa, P., Polito, V., & Pontieu, B. D. 2020, ApJ, 889, 124
Tian, H., DeLuca, E. E., Cranmer, S. R., et al. 2014a, Sci, 346, 1255711
Tian, H., Kleint, L., Peter, H., et al. 2014b, ApJL, 790, L29
Tian, H., Zhu, X., Peter, H., et al. 2018, ApJ, 854, 174
Tiwari, S. K., Alexander, C. E., Winebarger, A. R., & Moore, R. L. 2014, ApJL, 795, L24
Tiwari, S. K., Evans, C. L., Panesar, N. K., Prasad, A., & Moore, R. L. 2021, ApJ, 908, 151
Tiwari, S. K., Moore, R. L., Winebarger, A. R., & Alpert, S. E. 2016, ApJ, 816, 92
Tiwari, S. K., Panesar, N. K., Moore, R. L., et al. 2019, ApJ, 887, 56
Tiwari, S. K., van Noort, M., Lagg, A., & Solanki, S. K. 2013, A&A, 557, A25
Toriumi, S., Katsukawa, Y., & Cheung, M. C. M. 2017, ApJ, 836, 63
Vaiana, G. S., Davis, J. M., Giacconi, R., et al. 1973, ApJL, 185, L47
van Ballegooijen, A. A., & Martens, P. C. H. 1989, ApJ, 343, 971
van Driel-Gesztelyi, L., & Green, L. M. 2015, LRSP, 12, 1
Vissers, G. J. M., Rouppe van der Voort, L. H. M., & Rutten, R. J. 2019, A&A, 626, A4
Vissers, G. J. M., Rouppe van der Voort, L. H. M., Rutten, R. J., Carlsson, M., & De Pontieu, B. 2015, ApJ, 812, 11
Watanabe, H., Vissers, G., Kitai, R., Rouppe van der Voort, L., & Rutten, R. J. 2011, ApJ, 736, 71
Winebarger, A. R., Walsh, R. W., Moore, R., et al. 2013, ApJ, 771, 21
Yokoyama, T., & Shibata, K. 1995, Natur, 375, 42
Young, P. R., Tian, H., Peter, H., et al. 2018, SSRv, 214, 120
Zhukov, A. N., Mierla, M., Auchère, F., et al. 2021, A&A, 656, A35